DE GRUYTER Z. Phys. Chem. 2022; 236(6–8): 1013–1053

Contribution to Special Issue Dedicated to Paul Heitjans

Hendrik Wulfmeier*, Dhyan Kohlmann, Thomas Defferriere,
Carsten Steiner, Ralf Moos, Harry L. Tuller and Holger Fritze

Thin-film chemical expansion of ceria based solid solutions: laser vibrometry study

https://doi.org/10.1515/zpch-2021-3125
Received September 10, 2021; accepted October 18, 2021; published online November 11, 2021

Abstract: The chemical expansion of $Pr_{0.1}Ce_{0.9}O_{2-\delta}$ (PCO) and $CeO_{2-\delta}$ thin films is investigated in the temperature range between 600 °C and 800 °C by laser Doppler vibrometry (LDV). It enables non-contact determination of nanometer scale changes in film thickness at high temperatures. The present study is the first systematic and detailed investigation of chemical expansion of doped and undoped ceria thin films at temperatures above 650 °C. The thin films were deposited on yttria stabilized zirconia substrates (YSZ), operated as an electrochemical oxygen pump, to periodically adjust the oxygen activity in the films, leading to reversible expansion and contraction of the film. This further leads to stresses in the underlying YSZ substrates, accompanied by bending of the overall devices. Film thickness changes and sample bending are found to reach up to 10 and several hundred nanometers, respectively, at excitation frequencies from 0.1 to 10 Hz and applied voltages from 0–0.75 V for PCO and 0–1 V for ceria. At low frequencies, equilibrium conditions are approached. As a consequence maximum thin-film expansion of PCO is expected due to full reduction of the Pr ions. The lower detection limit for displacements is found to be in the subnanometer range. At 800 °C and an excitation frequency of 1 Hz, the LDV shows a remarkable resolution of 0.3 nm which allows, for example, the characterization of materials with small

---

Dedicated to Paul Heitjans on the occasion of his 75th birthday.

***Corresponding author: Hendrik Wulfmeier,** Clausthal University of Technology, Institute of Energy Research and Physical Technologies, 38640 Goslar, Germany,
E-mail: hendrik.wulfmeier@tu-clausthal.de
Dhyan Kohlmann and Holger Fritze, Clausthal University of Technology, Institute of Energy Research and Physical Technologies, 38640 Goslar, Germany
Thomas Defferriere and Harry L. Tuller, Massachusetts Institute of Technology, Department of Materials Science and Engineering, Cambridge, MA, 02139, USA
Carsten Steiner and Ralf Moos, University of Bayreuth, Department of Functional Materials, 95440 Bayreuth, Germany

levels of expansion, such as undoped ceria at high oxygen partial pressure. As the correlation between film expansion and sample bending is obtained through this study, a dimensional change of a free body consisting of the same material can be calculated using the high resolution characteristics of this system. A minimum detectable dimensional change of 5 pm is estimated even under challenging high-temperature conditions at 800 °C opening up opportunities to investigate electro-chemo-mechanical phenomena heretofore impossible to investigate. The expansion data are correlated with previous results on the oxygen nonstoichiometry of PCO thin films, and a defect model for bulk ceria solid solutions is adopted to calculate the cation and anion radii changes in the constrained films during chemical expansion. The constrained films exhibit anisotropic volume expansion with displacements perpendicular to the substrate plane nearly double that of bulk samples. The PCO films used here generate high total displacements of several 100 nm's with high reproducibility. Consequently, PCO films are identified to be a potential core component of high-temperature actuators. They benefit not only from high displacements at temperatures where most piezoelectric materials no longer operate while exhibiting, low voltage operation and low energy consumption.

Keywords: electro-chemo-mechanical actuation; electrochemical pumping cell; high temperature; laser Doppler vibrometry (LDV); praseodymia ceria solid solution; thin films.

1 Introduction

Chemical expansion in oxides is a well-known phenomenon. It originates from the incorporation or removal of oxygen out of the crystal lattice, typically driven by changes in the oxygen partial pressure of the surrounding atmosphere. This might occur either intentionally due to required changes in process parameters or due to chemical reactions associated with, e.g., a combustion process. Since chemical expansion is accompanied by mechanical stress, in order to minimize mechanical degradation, efforts are often made to avoid or suppress this chemo-mechanical effect as much as feasible. For example, multi-stack systems used in solid oxide fuel cells (SOFC) inherently see steep gradients in oxygen partial pressure between the air cathode and fuel anode that lead to corresponding strain gradients that can induce electrode delamination and/or electrolyte or electrode microcracking [1–3]. Furthermore, in addition to thermal and chemical expansion/contraction driven by local environmental conditions at the cathode and anode, solid oxide electrolysis cells (SOEC) suffer from electric field induced local modifications in oxygen vacancy concentration that can lead to even greater chemical expansion effects. It is thus clear that a detailed knowledge of the dependence of chemical expansion of relevant oxides on composition, temperature, atmosphere, etc., is needed for materials design and optimization for various applications in which oxygen stoichiometry varies under operating conditions. Aside from the potential negative impact that chemical expansion can have on mechanical stability of oxides, it can be used advantageously as electric field controlled mechanical actuators, as described in the following.

1.1 Motivation: electro-chemo-mechanical actuation

As mentioned above, chemical expansion occurs in a wide variety of non-toxic, low-cost and abundant oxide materials. Possible areas of application of such mechanical displacements include resistive nano-switches and a new generation of high-temperature actuators. For the latter chemical expansion may overcome the limitations of e.g. piezoactuators with large piezoelectric coefficients which in general are not operable at high temperatures as their Curie temperature rarely exceeds 400 °C [4, 5].

The market for piezoactuators has long been dominated by lead-based materials from the lead zirconate titanate (PZT) family [6]. More recently, for environmental reasons, lead-free alternatives have been extensively researched [7]. Alkali metal niobates, such as so-called KNN based materials, show comparably high piezoelectric coefficients with Curie temperatures of up to 460 °C. Materials showing higher Curie temperatures are mostly utilized in single crystalline form. Among those, $LiNbO_3$ is one with the highest piezoelectric coefficient of $d_{15} = 68$ pm/V [8]. However, stoichiometric $LiNbO_3$ is challenging to grow and its congruent composition shows tendencies for degradation above about 300 °C [9–11]. High-temperature stable crystals like those belonging to the langasite family or $GaPO_4$ show low piezoelectric coefficients. This makes them unsuitable for actuator applications [12–14].

In contrast materials like the praseodymia-ceria solid solution (PCO) shows an isothermal expansion of up to 0.4% at 650 °C for $Pr_{0.1}Ce_{0.9}O_{2-\delta}$ (PCO) [15]. Considering combined thermal and chemical expansion coefficients, expansion values of up to 1.5% are reported [16, 17]. Isothermal displacements originate from chemical expansion induced by changes in oxygen partial pressure or due to applied potentials within electrochemical cells. In contrast to piezoelectric actuators, reversible deflections on the order of 1% are already realized by the authors by application of voltages in the order of 1 V, orders of magnitude lower than that required for piezoactuators [18, 19]. Due to the finite high-temperature conductivity of piezoelectric materials, high potentials are typically required which result in significant losses and, thus, high energy consumption. Actuators based on chemical expansion of oxides are comparable to a Nernst cell. Here, no current flows in the equilibrium state corresponding to different states of strain. To induce changes in strain state, only low excitation voltages and corresponding currents are required, leading to low losses. This makes devices based on chemical expansion a promising low voltage/low energy alternative to piezoactuators, especially of interest for self-contained energy systems like those needed in e.g. microreactors. For such applications, not only is voltage and energy consumption of importance, but also actuator size. The large expansion coefficients of PCO allow for such thin films to be used in microactuators given that a thickness change of nanometers can already be realized by thin films with a thickness of only a few micrometers. However, the reported data on PCO thin-film properties in the literature remain limited.

Importantly, total displacements induced by thin films can be substantially enhanced by depositing the films on appropriate substrates [18, 19]. Here, chemical expansion in the films leads to mechanical stresses, which when transferred to the substrate, can result in additional bending of the combined system, consisting of substrate and film. The combined effect of total displacement, i.e. the sum of thickness change of the film and substrate bending, can exceed the film thickness change by several orders of magnitude.

In order to actively apply chemical expansion as a micro actuation scheme, reliable materials data needs to be acquired, and a deeper understanding of the defect mechanisms underlying chemical expansion in such thin films must be derived. Ceria, and its solid solutions, are known for their thermal, chemical and mechanical stability. However, the chemical expansion of thin layers of these materials has so far only been investigated sporadically. For this study, PCO thin films were chosen as they are known to show high chemical expansion [3] making them a promising high-temperature actuator material. Pure ceria thin films are introduced as reference where it is known that for $p_{O2} \geq 10^{-20}$ bar, only small degrees of expansion are expected [20, 21].

Previous investigations of the expansion of PCO thin films are published in [18] and [19]. The former presents a nanoindentation study for mechanical characterization of the film expansion at temperatures up to 650 °C, which is the upper operating limit of that measurement system. Bending of the samples due to chemical expansion of the film was demonstrated. In [19] the applicability of LDV to determine thin-film expansion and, in particular, film thickness changes at 720 °C were further demonstrated. These measurements were performed without variation of the applied potential and for a limited variation of the excitation frequencies (0.2–1 Hz). The same measurement system is now used in this work to extend the study by accessing the substrate bending and film thickness changes under more extensive conditions, including a wider range of oxygen partial pressures. Key benefits of the non-contact characterization method applied here is that no damage is induced to the films under study e.g. in contrast to nanoindentation, as well as the ability to access higher temperatures and a wider range of oxygen partial pressures ranging from highly oxidizing to highly reducing conditions.

1.2 Objectives of the work

In this work, the chemical expansion of praseodymia ceria solid solution (PCO) and ceria thin films on yttria stabilized zirconia (YSZ) substrates are investigated up to 800 °C. A key requirement for such chemo-mechanical expansion studies is to ensure that the measurement tool has as little of an effect as possible on the mechanical expansion of the layers. Therefore, the measurements are carried out utilizing a recently developed non-contact optical measurement technique, i.e. the Laser-Doppler Vibrometry (LDV). The chemical expansion of the films, and the induced sample bending, are measured *in operando* at higher temperatures than techniques like the aforementioned nanoindenter system could achieve.

By pursuing a full parameter study with respect to temperature (600–800 °C), excitation frequency (0.1–10 Hz) and applied voltage (0–0.75 V for PCO and 0–1.0 V for $CeO_{2-\delta}$) we can significantly extend the chemo-mechanical data on PCO and $CeO_{2-\delta}$ thin films which, to date, are limited or not available in the literature. The variation of the parameters aids in identifying the time constants, that in concert with given potentials, are needed to reach near equilibrium conditions.

Ceria is expected to show significantly lower chemical expansion than PCO in the anticipated parameter range given that the reduction of the Ce ion from the 4+ to 3+ state begins under much more highly reducing conditions than the corresponding reduction of the Pr ion. Therefore, it serves both as a model system to test the sensitivity of the newly developed LDV measurement system, as well as a reference material for the modified PCO system. This allows for direct access of the chemical expansion properties of thin PCO films over extended operating conditions, as well as, enables correlation with previous work on oxygen non-stoichiometry in PCO thin films obtained under more limited experimental conditions. Comparison with known defect models for PCO is intended to deepen insight into the operating mechanisms during film expansion and into the effective ion radii changes of cations and anions involved. For this purpose, an existing defect model for bulk PCO [22] will be used and adapted so that differences in the chemical expansion and the effective cation radii change between constrained thin films and freely expanding bulk PCO are identified.

More generally, this investigation opens new prospects for high-temperature thin-film actuators that operate with much reduced excitation voltages.

2 State of the art

2.1 Techniques for investigating chemical expansion and displacement of thin films

As far as the authors are aware, high-temperature LDV is the only technique presently available to detect chemical expansion in a direct non-contact mode. Its suitability for the detection of chemical expansion was demonstrated in [19] for PCO thin films up to 770 °C [23]. Furthermore, LDV is not only able to detect thin-film thickness changes generated by chemical expansion, but also the additional bending generated by mechanical stresses originated in the film and transferred to the substrate.

Dilatometry [24, 25] or high-temperature X-ray diffraction (HT-XRD) [26, 27] are well-established techniques to investigate expansion/contraction of bulk samples. Dilatometry requires sufficiently large samples to detect absolute displacements with good precision. Information gathered by X-ray diffraction is limited to the penetration depth of the radiation source used. This might be problematic for bulk samples if expansion in the near surface regions deviates from that within the inner volume of the specimens. HT-XRD is thus well suited for examining powder samples and sufficiently thin films. While HT-XRD benefits from being contactless, detection of film thickness change is largely limited to detecting lattice constant changes, but not induced bending of sample/substrate composites.

Nanoindentation, as applied by [18], does enable measurement of such induced bending, but unlike LDV, it is not contactless, leading potentially to film damage, including pin-holes in very thin films. Furthermore, indenters are typically limited to temperatures well below the 650 °C temperature limit achieved in the specially designed nano-indenter used previously by the authors [18]. On the other hand, the LDV technique applied in this study can achieve a high-temperature operability of more than 1000 °C while contactless and thus nondestructive.

2.2 Chemical expansion

Chemical expansion results from changes in oxygen nonstoichiometry, δ, in oxide materials of general composition $M_aO_{b\pm\delta}$. For ceria based solid solutions, the temperature and oxygen partial pressure (p_{O2}) dependence of nonstoichiometry has been widely studied [3, 28]. As discussed briefly above, oxygen vacancies created during exposure to reducing environments and/or increasing temperatures, are compensated by a change in the valence states of the cations [15, 29].

Figure 1 is a compilation of various literature data for PCO and undoped ceria. Data for bulk and thin-film ceria are taken from [30] and [31], respectively, while that for $Pr_{0.2}Ce_{0.8}O_{2-\delta}$ (bulk) and PCO (thin film) were published in [17] and [32], respectively.

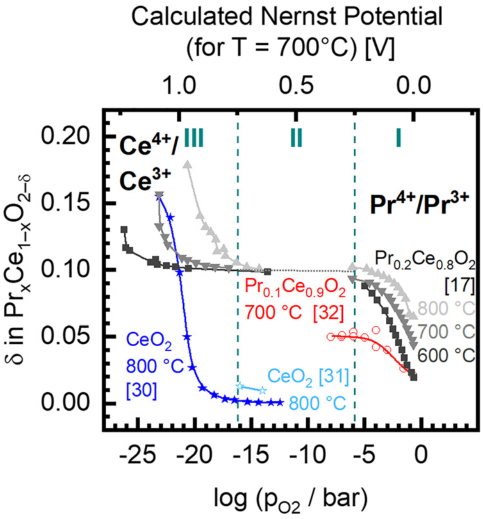

Figure 1: Oxygen nonstoichiometry δ dependence on p_{O2} in $Pr_xCe_{1-x}O_{2-\delta}$. The literature data for $Pr_{0.2}Ce_{0.8}O_{2-\delta}$ [17] are obtained from powders/bulk samples whereas the data for $Pr_{0.1}Ce_{0.9}O_{2-\delta}$ (PCO) were determined from thin films [32]. Undoped ceria data ($x = 0$) are shown for both bulk [30] and thin film samples [31]. For reference, the Nernst potential is calculated at 700 °C by Eq. (6). The indicated regions (I)–(III) show the ranges in which the valence changes of the different cations contribute to changes in nonstoichiometry: (I) Valence change of Pr^{4+}/Pr^{3+} – reversible process. (II) Nearly plateau-like behavior. (III) Valence change of Ce^{4+}/Ce^{3+}.

In the following, we examine the behavior of the oxygen nonstoichiometry of PCO in some detail. In particular, we note that the dependence of δ on oxygen partial pressure can be divided into three regions as indicated in Figure 1.

Region (I)

The formation of oxygen vacancies at higher p_{O2} can be described by the following defect relation:

$$2Pr_{Ce}^{X} + O_O^{X} \leftrightarrow 2Pr'_{Ce} + V_O^{\cdot\cdot} + \frac{1}{2}O_2\,(gas) \tag{1}$$

Here, Kröger–Vink notation is used. The lower index describes the location of the ion in the lattice. The upper index gives the relative charge of the ion with respect to its lattice position (′ = negative; · = positive x = neutral). Pr_{Ce}^{X} and Pr'_{Ce} are praseodymium ions located on cerium positions with fourfold and threefold positive charge. O_O^X and $V_O^{\cdot\cdot}$ represent oxygen ions and vacancies, respectively.

For near stoichiometric PCO, the Pr cations are mainly fourfold charged. As the oxygen vacancy concentration increases, increasing levels of Pr^{4+} are reduced to Pr^{3+}. This reaction is reversible [3, 15].

Region (II)

For intermediate p_{O2}, only small changes in the oxygen vacancy concentration occur leading to a nearly stable plateau in oxygen nonstoichiometry, δ. The p_{O2} limits of the plateau depend on the concentration of praseodymia in solid solution. A stable plateau is reached, when all of the Pr^{4+} ions are reduced to Pr^{3+} and Ce^{4+} has not yet begun to reduce to Ce^{3+}. The magnitude of δ in the plateau region thus shows a nearly linear dependence on x in $Pr_xCe_{1-x}O_{2-\delta}$. This explains the difference in the data sets obtained from [17] and [32]. Temperature does not influence the amount of praseodymium that can be reduced in this saturated regime. Therefore, for a given praseodymium concentration, no dependence of the value of δ in the plateau region with respect to temperature is found. However, temperature affects the oxygen activity and by this the reducibility of the Pr and Ce cations at a given oxygen partial pressure. The high and low limits in p_{O2} of the plateau region with respect to p_{O2} therefore do shift with temperature. In this ionic plateau region, the approximate electroneutrality expression is given by:

$$[Pr_{total}] \cong [Pr'_{Ce}] = 2[V_o^{\cdot\cdot}] \tag{2}$$

The total electrical conductivity is dominated by the migration of oxygen vacancies and thus the activation energy for electrical conduction is characterized solely by the oxide ion migration energy [33].

Region (III)

Under low p_{O2} conditions, a strong increase in δ is again observed. This originates from the fact that formed oxygen vacancies are now being compensated by changes in the valence state of the cerium rather than the praseodymium cations. An even stronger influence of temperature is seen compared to region (I) given the larger enthalpy needed to reduce Ce versus that of Pr [34]. In this work, region (III) is not further considered in the investigation of PCO, since the plateau serves as a reference for all measurements being temperature independent and not susceptible to minor changes in p_{O2}. Going into region (III) would result in a state that is strongly influenced by small changes in sample temperature or applied potential, and, by this, in oxygen partial pressure. For possible future actuator applications operation within region (II) is favorable as a constant displacement is desired that is influenced as little as possible by small disturbances of the external conditions.

For pure ceria, region (I) does not exist as no additional multivalent dopant cations to Ce like Pr exists. Instead, the plateau of region (II) is extended to high p_{O2} and is the consequence of fixed acceptor-like background impurities. High oxygen nonstoichiometry of undoped ceria comparable to PCO is reported at higher temperatures and/or lower p_{O2} (region III). A strong increase in nonstoichiometry is first seen in region (III) [35]. The CeO_{2-x} defect relation is given by [36]:

$$2\mathrm{Ce}_{\mathrm{Ce}}^{X} + \mathrm{O}_{\mathrm{O}}^{X} \leftrightarrow 2\,\mathrm{Ce}_{\mathrm{Ce}}' + \mathrm{V}_{\mathrm{O}}^{\cdot\cdot} + \frac{1}{2}\mathrm{O}_2\,(\mathrm{gas}) \tag{3}$$

The current state of the art focuses on three mechanisms that contribute to chemical expansion. In a recent review article, Schmitt et al. [28] conclude that probably no single simple explanation for chemical expansion exists, but that all three of the following explanations play some role.

1. The first proposed mechanism focuses on the fact that reduced praseodymium and cerium ions (Pr^{3+}/Ce^{3+}) have increased ionic radii on the order of 10% compared to Pr^{4+} or Ce^{4+}. The change in valence state thus induces a corresponding change in the lattice parameter [37].
2. The second is an electrostatic mechanism [16]. The release of oxygen ions under low p_{O2} leads to the formation of oxygen vacancies in the material. As a consequence, the neighboring cations surrounding the vacancies experience electrostatic repulsion and, thereby, a local increase in the lattice constant follows. These first two explanatory approaches are often seen as concurrent competing mechanisms [22].
3. The third explanatory approach is based on changes in the local symmetry around point defects. The formation of oxygen vacancies is no longer seen as the generation of isolated defects, but instead, especially for higher defect densities, (e.g. at very low p_{O2}, high dopant concentrations and/or high temperatures), defect clusters form. The growing concentration of reduced cerium cations $\mathrm{Ce}_{\mathrm{Ce}}'$ and oxygen vacancies $\mathrm{V}_{\mathrm{O}}^{\cdot\cdot}$ in undoped ceria and in PCO under highly reducing conditions increases the probability that they will combine to form associated intrinsic defect associates like dimers $(\mathrm{V}_{\mathrm{O}}^{\cdot\cdot}\mathrm{Ce}_{\mathrm{Ce}}')^{\cdot}$ or trimers $(\mathrm{Ce}_{\mathrm{Ce}}'\,\mathrm{V}_{\mathrm{O}}^{\cdot\cdot}\mathrm{Ce}_{\mathrm{Ce}}')^{\mathrm{x}}$ [38]. In trivalent doped ceria solid solutions, where, $\mathrm{D}_{\mathrm{Ce}}'$ is a trivalent dopant cation, additional extrinsic dimer $(\mathrm{V}_{\mathrm{O}}^{\cdot\cdot}\,\mathrm{D}_{\mathrm{Ce}}')^{\cdot}$ or trimer $(\mathrm{D}_{\mathrm{Ce}}'\,\mathrm{V}_{\mathrm{O}}^{\cdot\cdot}\,\mathrm{D}_{\mathrm{Ce}}')^{\mathrm{x}}$ and mixed trimer

defect complexes $(\mathrm{D}'_{\mathrm{Ce}}\,\mathrm{V}_{\mathrm{O}}^{\cdot\cdot}\mathrm{Ce}'_{\mathrm{Ce}})^{\mathrm{x}}$ may form under the same conditions [36]. Under more reducing conditions praseodymium in PCO solid solutions gets reduced to Pr^{3+} and the possibility of extrinsic and mixed defect complexes can occur for PCO as well. For high dopant concentrations, the formation of defect complexes is facilitated. The effective electrostatic charge of the individual defects is reduced for complexes with an oxygen vacancy in close proximity to two dopant or reduced cerium ions. Accordingly, defect complexes show a smaller volume, and thus smaller chemical expansion, than isolated defects; trimers even more than dimers [36]. Furthermore, the resulting charged defect complexes are attracted to one another, and exhibit binding energies that are a strong function of the dopant ion size. Small dopants show highest binding energies when the oxygen vacancy is in a first neighbor site while large dopants prefer the oxygen vacancy to be in a second neighbor site [39]. The latter is the case for the reduction of Pr^{4+} and Ce^{4+} ions, as in this study.

The wide majority of the literature on defect and transport in ceria is focused on bulk samples. Defect models and chemical expansion data for ceria based solid solution thin films are, on the other hand, limited. An expansion of about 0.28% for PCO thin films at 800 °C is reported in [40]. However, expansion in these PCO thin films was only characterized for a p_{O2} range between $10^{-3.8}$ bar and 10^{0} bar. Data for lower p_{O2} are not reported. The chemical capacitance of these PCO thin films was found to be larger than their bulk counterparts and the corresponding defect formation energies to be lower for the thin film case. As the chemical capacitance correlates with the oxygen vacancy concentration, this indicates that PCO thin films exhibit more oxygen vacancies than bulk specimens under the same p_{O2} and temperature conditions. This originates from the lower enthalpy of reduction for the Pr cations in the film, indicating that the film will be reduced easier/faster than the bulk [41]. The out-of-plane chemical expansion is found to be larger than the uniform chemical expansion of a bulk sample [40]. In a first approximation, the enhanced thin-film chemical expansion coefficient in the z-direction ε_{f} can be calculated from the known bulk chemical expansion coefficient ε_{b} [42]:

$$\varepsilon_{\mathrm{f}} \approx \varepsilon_{\mathrm{b}}\left(\frac{1+\nu}{1-\nu}\right) \tag{4}$$

with ν the Poisson's ratio. See also Appendix, Section 7.2. The main drawback is the limited knowledge of exact values for ν. In [40], an adapted bulk defect model was fitted to the experimental thin-film data. By slight variations of the other model parameters, nearly equally good fits for Poisson's ratio values in the range from $0.25 < \nu < 0.33$ were found.

2.3 Oxygen nonstoichiometry in PCO thin films

In materials like PCO, the oxygen nonstoichiometry δ is directly connected to the oxygen vacancy concentration:

$$\delta = \frac{[V_O^{\cdot\cdot}]}{[Pr_{0.1}Ce_{0.9}O_2]} \tag{5}$$

Thermogravimetry is commonly used to characterize the oxygen nonstoichiometry in bulk materials [3, 28, 43]. However, bulk nonstoichiometry data may deviate from thin-film data [44]. δ in PCO thin films was found to differ from that of the bulk, with $\delta_{\mathrm{film}} > \delta_{\mathrm{bulk}}$. This follows from a decreased enthalpy of reduction of 4.12 ± 0.25 eV for the PCO film, compared to 4.52 ± 0.37 eV for the bulk material [45].

For thin films, the sample mass is, in general, too small to measure with classical microbalance thermogravimetry. If the defect model of the material of interest is known, δ can be accessed instead by measurement of the chemical capacitance and subsequent correlations with temperature and p_{O2} dependences [46]. If no well-established defect model exists, however, direct investigative methods like the use of piezoelectric nanobalances are required. Specifically, special nanobalances, using stable high-temperature piezoelectric resonator materials, in which the dependence of the mass loss of thin films are investigated as functions of oxygen partial pressure and temperature by monitoring shifts in resonator resonance frequency, are required [32].

For PCO, reliable defect models have been reported on, therefore making both nanobalance and chemical capacitance approaches suitable. Published nonstoichiometry data for PCO films derived by both nanobalance [32] and chemical capacitance [46] are in good agreement.

2.4 Adjustment of oxygen activity

At sufficiently elevated temperatures, oxide materials tend to equilibrate with changes in temperature and the surrounding atmosphere in reasonable time scales. Oxygen incorporation or release is driven by changes in the surrounding oxygen partial pressure (p_{O2}). The oxygen activity in the material follows those external changes and approaches equilibrium. Alternatively, the oxygen activity in the films of interest can be adjusted using an oxide ion conductor as substrate that serves simultaneously as an oxygen pump, e.g. YSZ [19, 34]. The electrochemical pumping cell system of film and YSZ substrate is shown in Figure 2(a). It consists of: electrode / material of interest / oxygen pump / electrode.

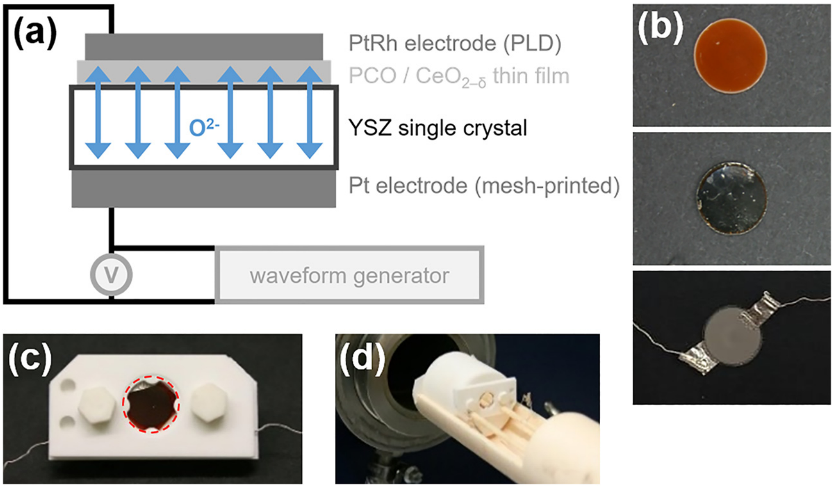

Figure 2: (a) Scheme of electrochemical pumping cell, consisting of a YSZ single crystalline substrate, Pt electrodes and PCO or ceria thin films. (b) Image of a PCO thin film. Top: Right after PCO deposition. Middle: A fully electrode-covered PCO thin film sample before measurements. Bottom: An electrode-covered sample after the measurement. Here, the platinum foils for contacting the platinum electrodes remain attached. (c) Sample installed in the alumina sample holder. The red dashed circle indicates the position of the sample. (d) Sample holder attached to the LDV measurement setup.

By applying a potential to the pumping cell, the effective p_{O2} in the film can be controlled. The correlation between applied potential U and oxygen activity at the interface between film and pump is approximated by the Nernst equation:

$$U = \frac{R\,T}{z\,F}\ln\left(\frac{p_{\mathrm{O2}}^{\mathrm{ref}}}{p_{\mathrm{O2}}}\right) \tag{6}$$

Here, R and F are the universal gas constant and the Faraday constant, respectively, and T is the temperature given in Kelvin. The reference oxygen partial pressure $p_{\mathrm{O2}}^{\mathrm{ref}}$ in this work is ambient air. z is the number of electrons transferred, being four for the case for O_2. To show the dependence between potential and oxygen activity, the potentials at 700 °C that correspond to the equivalent p_{O2} generated in the films are calculated and added to Figure 1 (top axis). Literature data and potentials in Figure 1 represent conditions of stationary states.

LDV measures displacement by analyzing phase and run-time differences between emitted and backscattered laser beams. Therefore, the sample has to be operated in a dynamic mode, with continuously varying dimensions. For this, a sinusoidal voltage signal can be applied to the pumping cell. The stationary state would then be approximated by very low excitation frequencies to the pumping cell. With the LDV used in this work, no chemical expansion for frequencies below 0.1 Hz are detectable. The excitation frequency was varied between 0.1 Hz and 10 Hz.

The focus of this work is on the plateau region (II) as indicated in Figure 1. The objective is to achieve an oxygen activity within the plateau. In order to ensure this, excitation potentials of $U_{\max}$ from 0.25 V to 0.75 V were selected for the PCO thin films. 0.75 V corresponds to the low-oxygen-activity end of the plateau. In this way, one is assured that the sample is not driven into region (III). The lowest potential of 0.25 V corresponds to the beginning of the plateau, as calculated by the Nernst equation assuming equilibrium conditions.

3 Experimental procedure

3.1 Sample preparation

3.1.1 Substrates: 8 mol-% YSZ single crystals were used as substrates and serve as the oxygen pump electrolyte. Double-side polished, square (10×10 mm^2) specimens with orientation of (100) were purchased (MTI corp., USA). In order to achieve circular symmetrical stresses in the samples for easier modelling of the bending of substrates and films, these substrates were machined into a circular shape with 10 mm diameter by ultrasonic milling (dama USF-300, Switzerland).

Thin films were prepared by pulsed laser deposition (PLD). The PLD targets used were prepared as described below.

3.1.2 PCO targets: The $Pr_{0.1}Ce_{0.9}O_2$ (PCO) PLD targets were synthesized using powder prepared by a co-precipitation procedure described in [47] Cerium nitrate $Ce(NO_3)_3$:$6H_2O$, and praseodymium nitrate $Pr(NO_3)_3$:$6H_2O$ (Strem chemicals, USA; purity: 99.99%) were dissolved in stoichiometric proportion (90/10) in deionized water at a concentration of 0.1 mol/L. The precipitation solution was prepared by dissolving ammonium carbonate in deionized water at a concentration of 0.5 mol/L. The amount of ammonium carbonate solution was prepared to have a molar excess of 2.5 as compared to the total amount of cations in the nitrate solution. The ammonium carbonate solution was poured into a vigorously stirred nitrate solution to initiate precipitation. The precipitate was subsequently filtered and washed four times in deionized water in a Buchner filter connected to a vacuum pump and dried at 100 °C for about 15 h, followed by calcination at 600 °C for 1 h with 2 K/min heating and cooling rate to obtain PCO oxide powder crystallized in the fluorite structure. The powder was subsequently pressed into a 30 mm diameter disk with a uniaxial press under a pressure of 1000 kg/cm^2. The pellet was sintered at 1500 °C for 6 h, followed by cooling at 1 K/min, to prevent crack formation, yielding a pellet with 97% density with respect to a theoretical density of 7.2 g/cm^3.

3.1.3 CeO_2 targets: The ceria targets for pulsed laser deposition (PLD) were prepared by using CeO_2 powder (99.99% purity, Chempur GmbH, Germany) which was first dried at 120 °C for 24 h to remove moisture. The powder was homogenized by planetary ball milling (Fritsch Pulverisette 5, Germany) at 400 rpm while using a 3.5 mol-% MgO hardened ZrO_2 crucible and 5 mol-% Y_2O_3 stabilized zirconia balls in two homogenization runs (2 min milling time, 15 min pause in between). Powder specimens of 2 g each were cold-pressed into pellets of approx. 13 mm in diameter using a hydraulic press (Raptor WPS 10C, Germany). A uniaxial force of 20 kN was applied for 10 min, followed by a 5 min pressure release. Subsequently, these pellets were sintered at 1650 °C for 12 h in a chamber furnace (Nabertherm LHT08/17, Germany) at a heating rate of 5 K/min and cooled down with the furnace time constant. Finally, the sintered material was subjected to heat treatment at 623 °C for 24 h (heating/cooling rate: 5 K/min). More details are given in [31].

3.1.4 PCO film deposition: The PCO films were deposited by high-temperature PLD at 650 °C using an UV excimer laser (Coherent CompexPro, USA) at 248 nm with a pulse length of 25 ns. The base pressure during deposition was 7×10^{-6} mbar while pure oxygen was constantly leaked into the PLD chamber during deposition, keeping the total pressure at 0.013 mbar during film growth and cooling steps. Repetition rate and pulse energy were 2 Hz and 150 mJ (power density of about 1.5 J/cm^2), respectively. While the heating rate was 10 K/min, the cooling rate was below 2 K/min to prevent possible film cracking.

3.1.5 CeO_2 film deposition: The ceria thin films were deposited by pulsed laser at room temperature using an UV excimer laser (Lambda Physics COMPex 205, Germany) at 248 nm with a pulse length of 25 ns. The base pressure during deposition was 1×10^{-6} mbar. Repetition rate and pulse energy were 10 Hz and 250 mJ, respectively. To compensate oxygen loss during deposition, post-annealing at 1000 °C for 10 h in ambient air was applied. Crystallinity of the films was examined by X-ray diffraction (Siemens D 5005, Germany). As-deposited films were amorphous. After annealing at 900 °C for 1 h, the films crystallized in face-centered cubic phase of the CaF_2-type ($Fm\bar{3}m$) [48].

3.1.6 Electrodes: Mesh-printed Pt electrodes (circular, diameter: 9.5 mm, thickness: ca. 3 μm) were applied to the backside of the substrates (platinum paste no. 64120410, Ferro Corp., USA; mesh size: 400 μm). The Pt electrodes were baked in ambient air at 1000 °C for 1 h. Ceria or PCO thin films were deposited onto the front side of the YSZ substrates by PLD as described above, see Figure 2(a). Both sample types, PCO and pure ceria, were covered with $Pt_{90}Rh_{10}$ top electrodes by using the same PLD system as for the ceria thin films (PLD target: m&k, Germany; 99.996% purity). Here, a repetition rate and a pulse energy of 30 Hz and 350 mJ, respectively, were used. An alloy of Pt and Rh was used instead of pure Pt to enhance the high-temperature stability [49]. Although thick mesh-printed Pt electrodes exhibit superior long-term high-temperature stability, thin PLD films of about 300 nm in thickness were used instead for the top electrodes as these are significantly smoother and, as such, exhibited higher reflectivity. The latter is required for the LDV measurements.

3.1.7 Sample characteristics: Film and electrode thickness, as well as their roughness, were investigated by tactile surface profilometry (Ambios XP-2, USA). Substrate thickness was measured by an inductive precision indicator (Mahr Extramess 2001, Germany). In this work three different kinds of samples are discussed. They differ in film material and substrate thickness. Their

Table 1: Samples used in this work.

sample name	Film material	Film thickness in µm	Substrate thickness in µm	Sample holder setup	Displacement on position (1)
PCO_{edge}	$Pr_{0.1}Ce_{0.9}O_{2-\delta}$	1.35	521	See Figure 3(a)	Maximal – film expansion plus max. amplitude of sample bending
PCO_{pin}	$Pr_{0.1}Ce_{0.9}O_{2-\delta}$	1.35	326	See Figure 3(b)	Minimal – film expansion only, negligible influence of sample bending
$CeO_{2-\delta}$	$CeO_{2-\delta}$	3.40	320	See Figure 3(a)	Maximal – film expansion plus max. amplitude of sample bending

characteristics are given in Table 1 together with the sample holder setup that these samples were measured in.

3.2 LDV measurements

The chemical expansion of the samples was determined by a high-temperature LDV setup developed within the authors' workgroup. A detailed description of this measurement device can be found in [19, 23]. The pumping cells are installed in an insulating alumina sample holder, see Figure 2(c) and (d). Top and bottom parts are held together by alumina screws and caps. Two different sample holder designs were used. The first is shown in Figure 3(a). Here, the sample is clamped at four points at the outer edge. By this design, the center of the sample remains unconstrained. The mechanical stress originated by the film thickness change causes a bending of the sample. In this setup the maximum amplitude for the deflection, which is the sum of film thickness change and sample bending, is found in the center of the sample.

The second sample holder, as shown in Figure 3(b), is a pin-support setup. The sample is supported only by a small pin (diameter: 1 mm) in the center of the sample. Here, the center of the sample is fixed while the outer area is free to bend. It is beneficial for this setup that the sample shows no bending in its center. Therefore, the displacement detected at the center should nearly totally originate from the film thickness change.

Top and bottom electrodes of the pumping cell are connected by thin platinum wires to a voltage source (Keysight 33509B-OCX, USA). Periodic pumping of the cell is achieved by applying a sinusoidal voltage between 0 V and U_{max} to the pumping cell (see Figure 4). In case of PCO, U_{max} is set to 0.25 V, 0.50 V and 0.75 V respectively. Considering the aforementioned p_{O2} regions (see Figure 1), 0.50 V is in the middle of the plateau-like region (II). 0.25 V and 0.75 V refer to the plateau region as well, being on their respective transitions to region (I) and region (III). Higher excitation voltages are omitted so not to exceed the plateau region with its defined and stable oxygen nonstoichiometry conditions. For ceria, an additional excitation voltage step of U_{max} = 1.00 V was added as ceria is not expected to show chemical expansion at high p_{O2}. As the current generated by the function generator is too low, an additional amplifier (I.E.D MAB M16-OM-1, Germany) was interposed. Excitation frequencies f_{exc} ranged from 0.1 to 10.0 Hz.

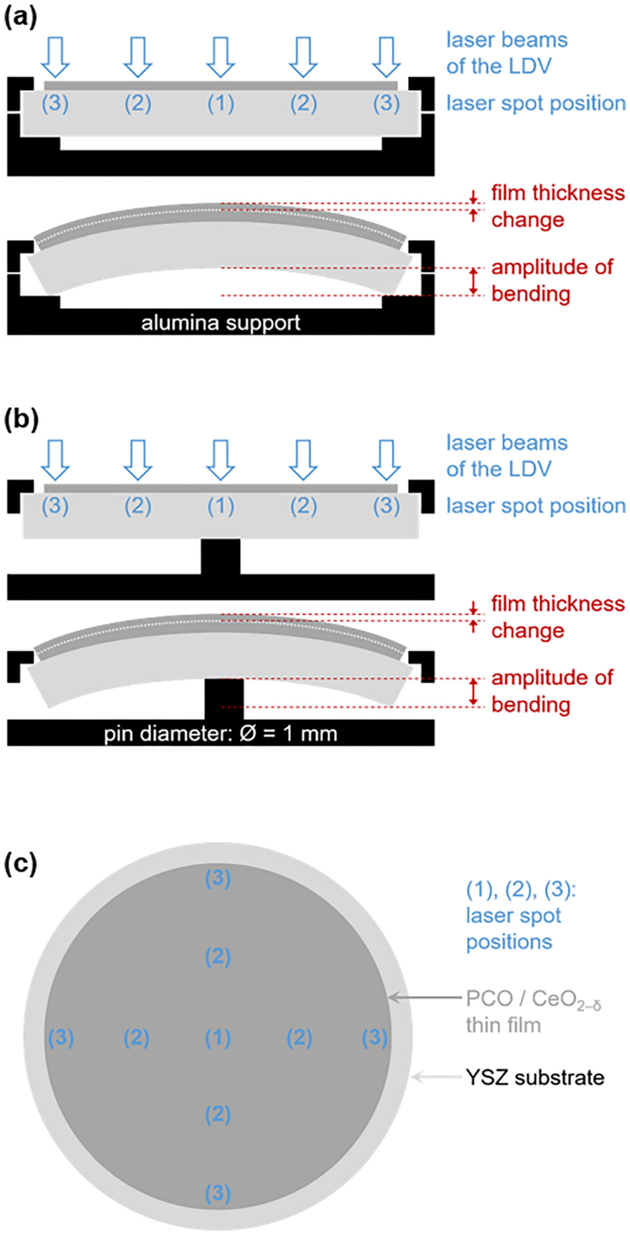

Figure 3: Scheme of sample holder for the (a) displacement characterization and indirect determination of the thin-film chemical expansion. Here, the sample is supported at the outer edge, (b) direct determination of the thin-film chemical expansion using a pin-support sample holder. (c) View from the top to illustrate the spot positions at which displacements were measured.

Very low frequencies are a better approximation of the stationary state and effective p_{O2} equilibrium conditions. At this point it should be mentioned that excitation frequencies lower than 0.1 Hz would be desirable, however, not achievable with the current setup due to an increasing noise level with decreasing frequency.

Thin-film expansion and sample bending are detected by optical interferometry. The interferometer is a single point LDV (Polytec GmbH OFV 505, Germany) operating on a He–Ne laser (wavelength: 632.8 nm). Depending on the frequency of the surface vibrations, resolution of displacements in the sub-nanometer range, perpendicular to the sample surface, can be achieved. Details are given in [19]. The LDV is placed outside of the furnace at a working distance of about 1 m between the laser head and sample. The resulting laser spot size is below 60 µm in diameter, thereby enabling sufficient lateral resolution during surface scanning of samples. A tilt mirror in the laser beam path allows for scanning of the sample surface. Positioning accuracy on the sample surface is about 1 µm, which means that lateral resolution is determined by the laser spot size. The scanning length ranges up to about 15 mm.

The evaluation of the measurement data is based on a frequency resolved analysis that is performed by calculation of the vibration amplitude from the time dependent LDV signal using a fast Fourier transformation (FFT). The experimental setup and the data evaluation are given in detail in [19] and [23].

Different sample spots are compared. In the following, three specific positions are defined as indicated in Figure 3:

- Position (1): Center of sample. For the sample holder configuration shown in Figure 3(a), this is the spot with the highest amplitude of sample bending and film thickness change. For the pin-support setup, Figure 3(b), the sample bending is largely negligible at this position. The detected displacements reflect the film thickness change more-or-less directly.
- Position (2): The measurement spots of position (2) are located on a circle of half the radius of those of position (3).

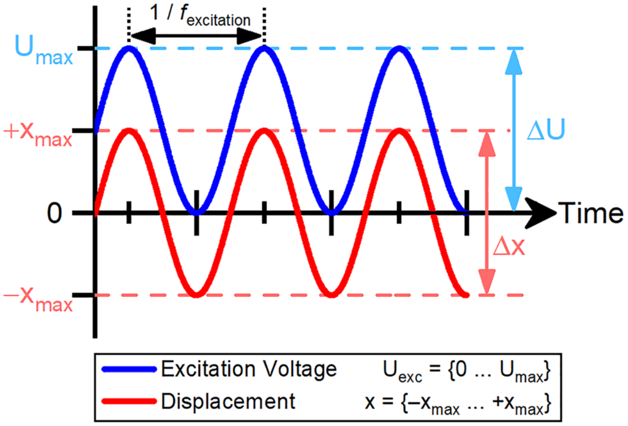

Figure 4: Correlation of the excitation and displacement signal. A sinusoidal signal with constant excitation frequency is applied between 0 V and the maximum excitation voltage, U_{max}. U_{max} represents the peak-to-peak potential of the excitation signal. In contrast, the signal of the LDV (displacement) oscillates symmetrically around zero.

- Position (3): At the outer edge. The measurement spots correlating to position (3) are placed so that the laser spot is just within the outer diameter of the PtRh top electrode. The impact of the sample holder setup is vice versa to position (1).

The sample holder is inserted into a tube furnace (Carbolite Gero HTSS 75-180/16, Germany). All measurements are performed in ambient air and within a temperature range from 600 °C to 800 °C. At temperatures below 600 °C, no film thickness change could be detected at excitation frequencies ≥0.1 Hz. Higher temperatures are omitted as PCO is reported to show decreasing chemical expansion at temperatures above 800 °C [15, 29]. To reduce stress in the samples, heating and cooling rates were limited to 3 K/min.

A type B thermocouple placed in close vicinity to the sample and connected to a digital voltmeter (Keithley DVM 2000, USA) is used to detect the sample temperature.

4 Experimental results

4.1 Excitation frequency dependence of chemical expansion for $Pr_{0.1}Ce_{0.9}O_{2-\delta}$ and $CeO_{2-\delta}$ thin films

4.1.1 PCO coated cells

Figure 5 shows the displacement dependence on excitation frequency of two PCO and ceria coated samples for excitation voltages described in Section 2.4 and given temperatures. The upper four graphs are depicting the maximum displacement detected on the respective samples, i.e. the sum of film thickness change and sample bending. For PCO_{edge} (closed symbols) and ceria (star-shaped symbols), displacement is detected in the center of the sample at position (1), compare Figure 3. For PCO_{pin} (open squares), the maximum deflection is detected at the most outer edge of the sample, i.e. position (3). For comparison, the respective data obtained for sample PCO_{pin} at position (1) are depicted as well (blue curve at bottom). Compared to their counterparts at position (1), these values show a smaller displacement by about 1.5–2 orders of magnitude. This major difference in the magnitude of displacement is expected given that measurements made at PCO_{pin} position (1) reflect changes in film thickness only with the effect of sample bending being largely negligible for these data points.

All graphs depicted in Figure 5 show a similar trend, i.e., increased displacement with decreasing excitation frequency. For low frequencies, displacement appears to approach a maximum saturation value. This indicates that the samples are near to reaching their equilibrium state already at 0.1 Hz.

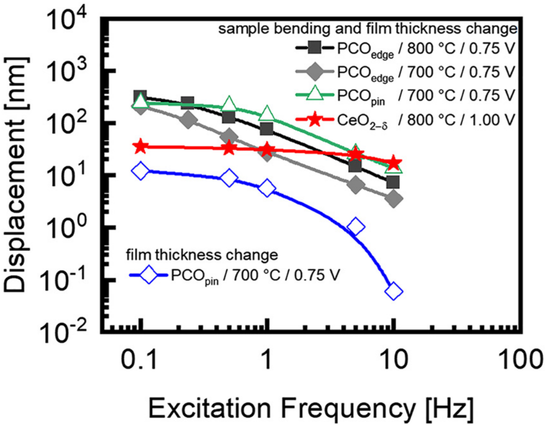

Figure 5: Frequency dependent displacement of PCO and $CeO_{2-\delta}$ thin films. Symbols: Closed squares – PCO_{edge}, closed stars – $CeO_{2-\delta}$, open symbols – measurements using pin-support sample holder, open squares – measurements at position (3) represent maximum displacement for this kind of sample support, triangular symbols – displacements detected at position (1), directly above the pin support. See text for details.

4.1.2 $CeO_{2-\delta}$ coated cells

On first impression, the chemical expansion of ceria and PCO appear to be comparable in magnitude, particularly at higher frequencies. However, it shall be mentioned that the $CeO_{2-\delta}$ graph shown in Figure 5 reflects data measured at a potential of 1.0 V, higher than those used for the PCO thin films. At lower potentials no data could be obtained for an excitation frequency of 0.1 Hz due to an insufficient signal to noise ratio (see Figure 6). This is also evident for measurements at positions (2) and (3), where the expected displacements are significantly lower. This was also visible in the measured data at these positions, which were hardly distinguishable from the noise level except at the highest applied voltage of 1.0 V. Therefore, in the following, only the maximum displacement detected at position (1) is discussed in detail.

Ceria sample displacement measurements were limited to T ≥ 800 °C due to poor signal to noise ratios at lower temperatures. The maximum displacement of ceria at 800 °C as a function of excitation frequency and voltage is given in Figure 6. The ceria sample shows a similar trend to PCO with respect to the excitation frequency dependence of displacement, including the tendency to reach a constant displacement at low frequencies suggesting the ability to reach a near

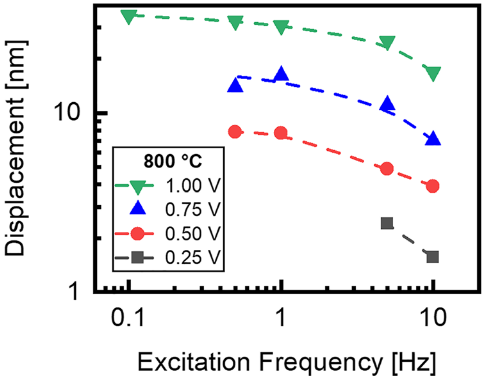

Figure 6: Displacement of ceria thin film at 800 °C as function of excitation voltage and frequency.

equilibrium state following changes in effective p_{O2}. The influence of the excitation frequency on the $CeO_{2-\delta}$ coated sample is, however, observed to be less pronounced than on the PCO coated samples.

4.2 Temperature and excitation voltage dependence of the chemical expansion

Displacement measurements are reported for the PCO samples over the temperature range from 600 °C to 800 °C. Below 600 °C, poor signal to noise levels limited meaningful data collection. For completeness, raw displacement data as a function of excitation voltage for different temperatures are shown in Figure 7 with all of these data obtained for PCO_{edge} at position (1).

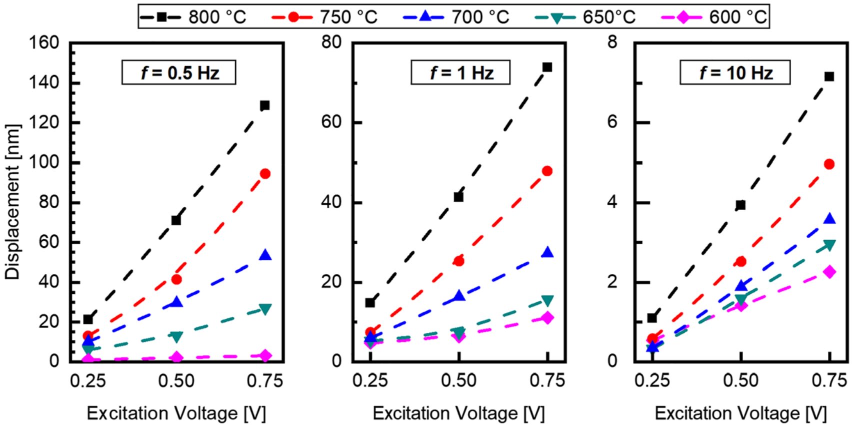

Figure 7: Temperature dependence of displacement of PCO sample depicted in Figure 5 versus excitation voltage shown for three different excitation frequencies: (a) 0.5 Hz, (b) 1.0 Hz, and (c) 10 Hz. Displacement increases with temperature and varies nearly linearly with excitation voltage.

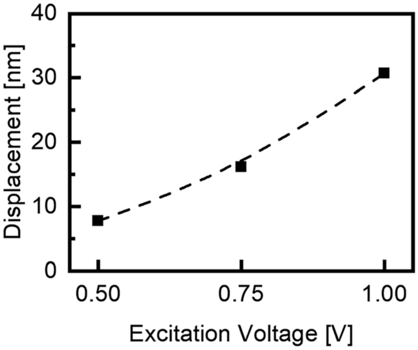

Figure 8: Displacement of $CeO_{2-\delta}$ sample at 800 °C as a function of excitation voltage. The maximum displacement in the center of the sample, i.e. position (1), is depicted. The excitation frequency is 1.0 Hz.

The dependence of the displacement on excitation voltage for $CeO_{2-\delta}$ is given in Figure 8. It shows a comparable trend as PCO. It shall be mentioned that for $CeO_{2-\delta}$ no data are shown for $U_{max} = 0.25$ V given poor signal to noise ratios at this excitation voltage.

4.3 Spatial distribution of displacement

To investigate the spatial displacement distribution, measurements at other locations as indexed in Figure 3 were also conducted, in addition to those performed at the center of the sample. The data obtained for PCO_{pin} at 700 °C, and under an applied excitation voltage of 0.75 V, are shown in Figure 9. To demonstrate that significant curvature from center to edge is observed, not only for low excitation frequencies, but also for high frequencies, the data were split into two graphs. Figure 9(a) depicts the higher frequencies from 10 Hz down to 1 Hz, while Figure 9(b) shows the lower frequencies between 1 Hz and 0.1 Hz. The data set for 1 Hz is given in both figures to allow for a better comparability. At position (1), the smallest displacement is detected, being only a few nanometers even for low frequencies. It is assumed that these values represent the thin-film thickness changes more-or-less directly. As the only support point in this sample holder is placed directly under position (1), no significant sample bending should have occurred there. Following the radius to the outer edge of the sample, the effect of stress originating from film expansion can be seen. An additional component contributes to the displacement, which is the bending of the sample. As expected, the bending, and by this the total displacement, increases with increasing distance to the center of the sample.

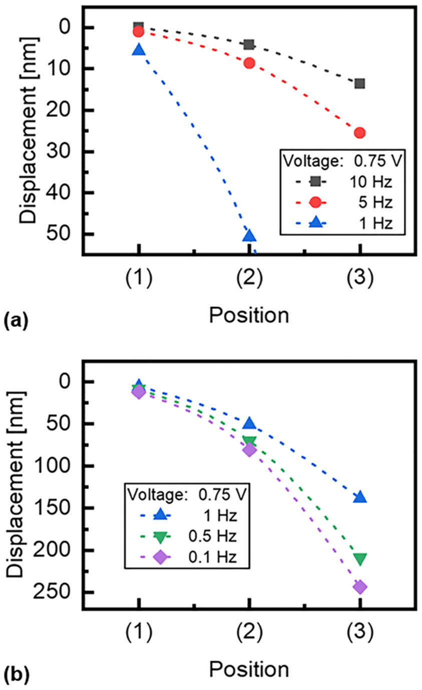

Figure 9: Displacement dependence on radius of the PCO_{pin} sample depicted in Figure 4. $T = 700$ °C. (a) Displacements for higher frequencies of 1–10 Hz. (b) Displacements for low frequencies of 0.1–1.0 Hz. The frequency of 1 Hz is shown in both graphs for comparison. The measurement positions are indicated in Figure 3.

Figure 10 shows results obtained for a similar investigation of the PCO_{edge} sample. Here, nine spots on the sample surface are evaluated, see Figure 3(c). A circular symmetry can be observed for all parameter sets, with displacement amplitudes for the excitation frequencies of 0.1 Hz and 1 Hz depicted in Figure 10. To represent the upward curvature of substrate bending, spherical surface segments are fitted to the data. The lines are spherical segment fits along the respective intersects. For both excitation frequencies, a similar curvature is observed, mainly differing in the total amplitude, being consistent with prior data presented in Figures 5, 6 and 9.

The spatial distribution of the displacement amplitude of the ceria thin film is depicted in Figure 11. Measurement conditions are ambient air at 800 °C, an excitation voltage of 1.00 V and an excitation frequency of 1.0 Hz. The $CeO_{2-\delta}$ coated sample shows a similar distribution and circular symmetry as found for the PCO sample.

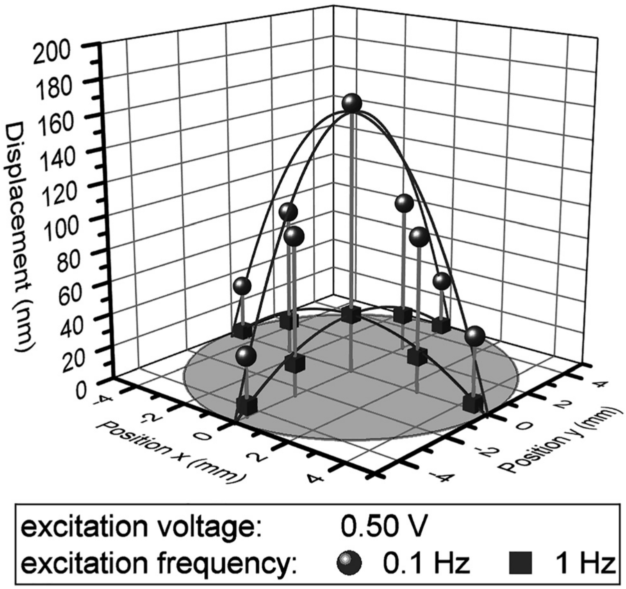

Figure 10: Spatial distribution of the displacement amplitude of the PCO_{edge} sample. Conditions: Ambient air, 800 °C, excitation voltage 0.50 V. The excitation voltage modulation frequency is 1.0 Hz (cubes) and 0.1 Hz (spheres), respectively. A similar distribution and circular symmetry for both excitation frequencies is found.

5 Discussion

Summarizing the observations for trends in PCO and $CeO_{2-\delta}$ chemical expansion, film thickness change and displacement increase with (1) excitation voltage, (2) increasing temperature and (3) decreasing excitation frequency.

These dependencies are expected for dynamic operation of the electrochemical oxygen titration cell. The observed dependence on frequency indicates that equilibrium conditions are not achieved for high frequencies and low potentials in these PCO and $CeO_{2-\delta}$ films under study. As displacement continues to increase with excitation voltage for low potentials and high frequencies, this informs us that the plateau, i.e. region (II) in Figure 1, has not yet been reached. The related data points still belong to region (I). As a consequence, the maximum displacement under equilibrium conditions, i.e. the substrate bending and the layer thickness change, might be larger.

The reason for this might be the formation of space charge zones at the interfaces (film/substrate, film/electrode, substrate/electrode) [50–52]. Accordingly,

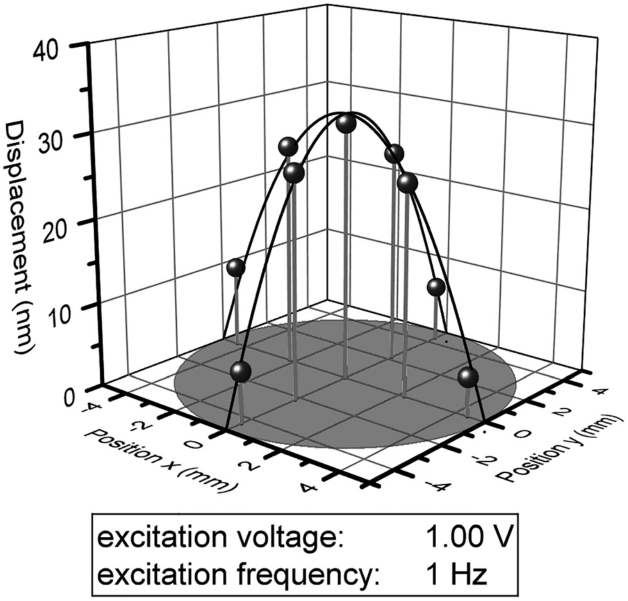

Figure 11: Spatial distribution of displacement amplitude of $CeO_{2-\delta}$ coated sample. Conditions: Ambient air, 800 °C, excitation voltage 1.00 V, excitation frequency 1.0 Hz. $CeO_{2-\delta}$ shows a similar distribution and circular symmetry to that of the PCO samples (see Figure 10). Note the lower total displacement despite a thicker film and thinner substrate.

the effective pumping voltage across the YSZ substrate is lower than the applied voltage due to voltage drop in the $CeO_{2-\delta}$ or PCO film and at the interfaces of the YSZ substrate. Therefore, the actual oxygen activity in the electrochemical cell might be lower than expected from the Nernst equation for a given applied voltage. Alternatively, the assumption that no leakage of the electrochemically inserted oxygen out of the film through the top surface of the PCO film exposed to the atmosphere may not hold. In that case, the effective p_{O2} in the film may be higher than expected from the Nernst equation (Eq. (6)). In future studies, oxygen impermeable films, e.g. MgO, will be deposited on these outer surfaces to mitigate against such potential leakage contributions. Lower frequencies and higher temperature represent measurement conditions that are closer to the calculated activities. Low frequencies allow for more time for the film to approach equilibrium conditions. Higher temperatures lead to increased oxygen diffusion constants for both YSZ [53] and PCO [54], and thus, a more rapid approach to achieving the expected oxygen activity inside the PCO. Further experiments to determine the effective pumping voltage and, thereby, the oxygen activity are part of the ongoing research.

The observed temperature dependence of the displacement supports this conclusion. Increased mobility of oxygen ions and, potentially, higher effective pumping voltages, push the films closer to equilibration or saturation state in region (II). Prior investigations revealed that the limiting kinetics are related to the rate in which oxygen can be provided through the YSZ electrolyte, not diffusion within the PCO thin films [18, 51]. For example, the oxygen diffusion coefficient for YSZ in the temperature range considered in this work ranges from 5×10^{-9} cm^2/s (at 600 °C) to 7×10^{-8} cm^2/s (800 °C) [53]. The increase by more than one order of magnitude allows for faster oxygen transport and, consequently, for higher displacements within a given period of time as long as equilibrium has not yet been reached.

5.1 Comparison of results for thin film PCO and ceria

At first glance, the displacements shown in Figure 12 for the PCO and $CeO_{2-\delta}$ coated samples seem to be on the same order of magnitude. However, three aspects need be mentioned: The $CeO_{2-\delta}$ coated sample has a film thickness which is about 2.5 times the PCO film thickness. The film is deposited on a comparably thin substrate that should show stronger bending than the thicker substrate used for PCO_{edge}. Furthermore, the excitation voltage applied is 1.0 V and, thereby higher than for PCO. Despite these three factors, the total displacement of the $CeO_{2-\delta}$ coated sample is still lower than the total displacement of PCO. This indicates that the chemical expansion of ceria is significantly smaller compared to that of PCO.

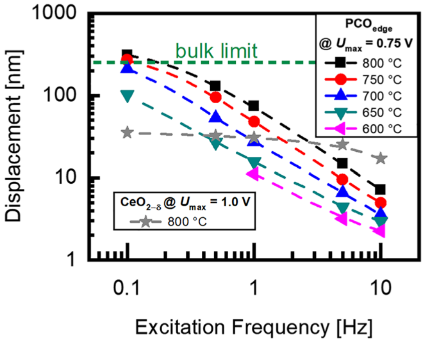

Figure 12: Displacement due to bending in dependence of the excitation frequency of PCO_{edge} and $CeO_{2-\delta}$ (star symbols). The displacement, which decreases with increasing frequency, approach a maximum for very low frequencies. For comparison, the bulk limit of a corresponding non-constrained PCO bulk sample is shown as dashed line.

To compare the displacement D that was caused either by bending of the PCO_{edge} or the $CeO_{2-\delta}$ samples, measurements taken under the same conditions ($T = 800$ °C) are depicted in Figure 13. For each material, data from two curves for an excitation voltage of 0.50 V and 0.75 V, respectively, are shown. To ensure comparability, the ceria data are corrected for film t_f and substrate thickness t_s of the PCO sample using the first-order approximations of $D \sim t_f$ and $D \sim 1/t_s^2$ according to the Stoney model (see Appendix, Section A.1). A significantly higher displacement for PCO by 1.5–2 orders of magnitude is found. As the material properties for the substrates and the effective pumping voltage are expected to be nearly identical, the higher displacement is attributed to the large inherent chemical expansion of the PCO films. Considering the p_{O2} applied, the higher displacement of PCO agrees with literature data for bulk materials. For bulk PCO an isothermal chemical expansion of up to 0.4% is reported [15, 36], compared to <0.01% for $CeO_{2-\delta}$ [22]. This relatively small expansion of $CeO_{2-\delta}$ is valid for the p_{O2} range of this work, i.e., from 0.21 down to 10^{-17} bar. For lower p_{O2} or higher temperatures $CeO_{2-\delta}$, shows a significantly higher chemical expansion coefficient. For an oxygen partial pressure of about 10^{-20} bar, the chemical expansion increases to 0.3% (800 °C) and to >1% (900 °C) respectively [55].

5.2 Displacement multiplication effect

The total displacements D detected by LDV are the sum of the film thickness change c_f and sample bending b. For constrained films, the expansion

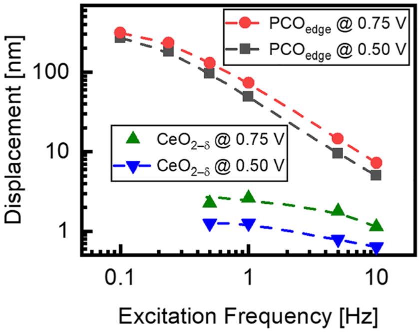

Figure 13: Total displacement, i.e. sum of bending and film-thickness change, of the samples PCO_{edge} and $CeO_{2-\delta}$. Corresponding data sets obtained for 0.50 V and 0.75 V at 800 °C are compared. The ceria displacement D is corrected for film t_f and substrate thickness t_s (see below: $D \sim t_f$, $D \sim 1/t_s^2$). A significantly higher bending for PCO by up to two orders of magnitude is found.

perpendicular to the plane of the substrate c_f is larger than the length change c_b of a free body consisting of the same material. The relation $c_\mathrm{f}/c_\mathrm{b}$ is discussed in Appendix, Section A.2. For thin-film PCO used here, a factor of $c_\mathrm{f}/c_\mathrm{b} \approx 2$ is found. In addition, the chemical expansion generates stresses in the film and leads to a substrate bending b. The relation between b and c_f is determined experimentally, see Section 5.3. Values of more than 30 are found for the ratio b/c_f.

To correlate the total displacements D with the related length change of a free body, a multiplication factor ξ is introduced:

$$\xi = \frac{D}{c_\mathrm{b}} = \frac{c_\mathrm{f} + b}{c_\mathrm{b}} \tag{7}$$

Taking $c_\mathrm{f}/c_\mathrm{b} = 2$ and $b/c_\mathrm{f} = 30$ a factor of $\xi = 60$ results. The quotient D/ξ corresponds to the minimum detectable length change of a free body. For the given LDV system, the resolution for the displacement D at 800 °C and 1 Hz is therefore calculated to be below 0.3 nm under ideal conditions. A related displacement c_b for a free body of 5 pm results even under challenging high-temperature conditions at 800 °C!

This displacement is on the same order of magnitude as accessible by techniques like electrochemical strain microscopy (ESM) which is based on atomic force microscopy (AFM). Sensitivities for ESM of about 3–4 pm are reported [56]. However, this resolution is obtained only near room temperature and not for the challenging high temperature conditions (up to ~1000 °C) at which the LDV system is operating.

According to the Stoney model, the bending is correlated to film thickness ($b \sim t_\mathrm{f}$) and substrate thickness ($b \sim 1/t_\mathrm{s}^2$), see Appendix, Section A.1. Considering this, an increase of ξ, and thus, further increases in resolution for c_b remain possible with the use of thicker films and/or thinner substrates.

5.3 Indirect determination of chemical expansion of PCO thin films

The Stoney model, see Appendix, Section A.1, can also be applied to the displacement mapping shown in Figures 10 and 11 where a uniform chemical expansion and a uniform curvature over the whole sample is assumed. Consequently, the film thickness change c_f and the mechanical stress are independent of the position on the sample. The displacement due to sample bending b and the total displacement D in the center depend on the radius of the sample. A related scheme is shown in Figure 14. For two points, e.g. in the center of the sample ($r = r_0$) and at the radius r_i, the displacement is calculated to be:

$$D(r_0) = b(r_0) + c_f \Leftrightarrow D_{max} = b_{max} + c_f \tag{8}$$

and

$$D(r_i) = b(r_i) + c_f \tag{9}$$

The film thickness change c_f is calculated using these measured values for D_{max} and D_i and the known radii:

$$c_f = \left(1 - \frac{r_s^2}{r_i^2}\right) D_{max} + \frac{r_s^2}{r_i^2} D_i \tag{10}$$

Here, r_s is the radius of the substrate. For 0.1 Hz, as depicted in Figure 10, a total displacement of $D_{max} = 162.3$ nm is measured. The calculated contributions of sample bending and thin-film expansion are $b = 155.2$ nm and $c_f = 7.1$ nm. This sample was grown on one of the thicker substrates (520 µm). In spite of this, the ratio b/c_f is already at a value of 18.9 and the ratio D/c_f is 22.8. In other words, for this given geometry a thin-film expansion of only a few nanometers results in a total displacement of more than 20 times larger than the film thickness change. In relation to c_b, this increases to a factor of ξ close to 45.

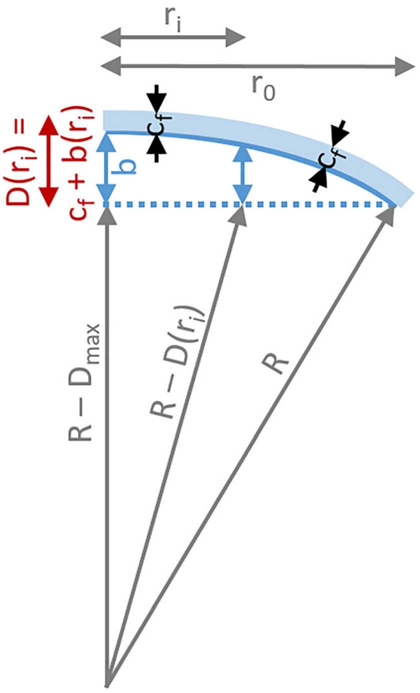

Figure 14: Scheme for the indirect determination of the film thickness change c_f. The maximum amplitude of sample bending is denoted by *b*. *D* is the sum of film thickness change c_f and sample bending *b*. The sample radius is denoted as *r*, the curvature radius as *R*.

The in-plane stress component for the PCO film that generates this sample bending is 270 MPa; for calculation see Appendix, Section A.1.

The experimental data measured at position (1) of the PCO_{pin} sample mainly reflect the thin-film expansion. As the pin-support has a finite diameter of 1 mm, a small contribution of the bending remains present. The bending contribution is approximated by fitting a circle function to the data shown in Figure 9. At position (1), a displacement of 12.1 nm is measured for an excitation frequency of 0.1 Hz and an excitation voltage of 0.75 V. The contribution of the bending is 4.7 nm. This results in a film thickness change of $t_f = 7.4$ nm and a multiplication factor of $\xi = 66.2$.

As expected for the given conditions, for undoped ceria the chemical expansion is much lower. A comparable film thickness change is measured using a film of 2.5 times that of the PCO film thickness. Despite a similar substrate thickness as used for PCO_{pin} and a higher excitation voltage of 1 V, a ratio of only $\xi \approx 10$ is detected.

Furthermore, the chemical expansion coefficient

$$\epsilon = c_f / t_f \tag{11}$$

is calculated from the thin-film expansion data. For PCO_{edge}, the value is $\varepsilon_{edge} = 0.53\%$. For PCO_{pin}, it is only slightly higher with $\varepsilon_{pin} = 0.55\%$. These differences are regarded as insignificant with respect to measurement uncertainty (compare Appendix, Section A.4).

Both experimental values, ε_{edge} and ε_{pin}, are higher compared to the literature values for bulk PCO ($\varepsilon_{bulk} = 0.4\%$ [15]). The smaller values for bulk PCO are expected as these samples are not constrained, meaning that the chemical expansion can propagate uniformly in all three spatial directions. In our work, the films are constrained in the plane of the substrate, while the only free direction is perpendicular to the surface. Therefore, it is a reasonable assumption that the chemical expansion in the X-Y plane is reduced in favor of an increased chemical expansion along the unrestrained Z-direction.

In the following section, a model is presented to correlate this anisotropic expansion of PCO thin films with the isotropic expansion of bulk PCO.

5.4 Correlation of thin-film chemical expansion and bulk chemical expansion by modelling the effective cation and anion radii change

To reach a deeper insight in the processes that lead to chemical expansion in PCO thin films, the defect mechanisms and their impacts on the effective ionic radii are investigated. To correlate the film thickness change determined in this work with literature models for the chemical expansion of bulk PCO, we adapt a model presented in [22]. In this defect model, the chemical expansion is described by calculating the change of the Shannon radii of the cations and anions and correlating this to the oxygen nonstoichiometry.

The calculations given below compare the chemical expansion and the ion radii change between the p_{O2} conditions of ambient air and the plateau (see Figure 1). For bulk PCO, both conditions are well-known in the literature with respect to oxygen nonstoichiometry and chemical expansion. For the PCO thin films investigated in this work, these conditions correspond to applied potentials of 0 V (ambient air) and 0.75 V (plateau region).

The first step is to determine oxygen non-stoichiometries in ambient air and for the plateau region (II). For this, the data of this study are correlated with prior investigations presented in [32]; for details, see Appendix, Section A.3. Following that, the total volume expansion of the films in this work is calculated. A theoretical effective expansion coefficient $\varepsilon_{\mathrm{eff}}$ is introduced to compare the uniaxial volume expansion of a constrained thin film with the unconstrained bulk expansion in three dimensions. $\varepsilon_{\mathrm{eff}}$ is further transferred to an effective nonstoichiometry in the films δ_{eff} and included in the defect model presented in [22] in order to calculate the effective cation and anion radii in the PCO thin films of this work.

5.4.1 Volume expansion of thin-film PCO and corresponding effective bulk expansion

In the following it is assumed that the full chemical expansion takes place in the Z direction, i.e. perpendicular to the substrate plane. To motivate this simplification, lateral film expansion is calculated first and compared to the thin-film expansion out-of-plane as determined by LDV.

The lateral expansion can be accessed through the bending of the substrate. Comparing the arc segment of the bent sample with the flat sample, an in-plane expansion coefficient of about $\varepsilon_{xy} = 1.4 \times 10^{-9}$ is found. This is by more than six orders of magnitude smaller than the out-of-plane expansion coefficient $\varepsilon_z = 5.3 \times 10^{-3}$. Therefore, the approximation of considering solely the out-of-plane film expansion is well justified.

With this simplification the volume expansion of the constrained $\mathrm{PCO}_{\mathrm{edge}}$ film is 0.53% along the *Z* axes and 0% in the *X*-*Y* plane. To compare this with an unconstrained bulk sample, a perfect cube with the same volume expansion is imagined. The related isotropic expansion in only one dimension results in an effective expansion coefficient $\varepsilon_{\mathrm{eff}} = 0.18\%$ in comparison with the bulk expansion.

5.4.2 Effective Shannon radii in PCO

The effective cation (r_{cation}) and anion radii (r_{anion}) are defined according to [16]:

$$r_{\text{cation}} = x r_{\text{s}} + (1 - x) r_{\text{h}} \tag{12}$$

$$r_{\text{anion}} = (1 - 0.25x) r_{\text{o}} + 0.25 x r_{\text{v}} \tag{13}$$

with r_{o} the radius of the oxide anion, r_{v} the radius of the oxygen vacancy, r_{h} the radius of the tetravalent host cation, and r_{s} the substitutional tetravalent cation. The parameter x stands for the fraction of trivalent cation substituting for tetravalent cations during expansion as in $Pr_x^{3+}Pr_{0.1-x}^{4+}Ce_{0.9}^{4+}O_{2-0.5x}^{2-}$. The relationship from the fraction parameter x to the oxygen nonstoichiometry δ is:

$$\delta = \frac{x}{2} \tag{14}$$

Out of these equations, the chemical expansion coefficient ε is calculated by:

$$\varepsilon = \frac{(r_{\text{cation}} + r_{\text{anion}}) - (r_{\text{h}} + r_{\text{o}})}{r_{\text{h}} + r_{\text{o}}} \tag{15}$$

The values for the oxygen vacancy radii are taken from [22]. All other Shannon radii are taken from [57]. Due to the crystallographic structure of PCO, the radii with coordination numbers VIII (cations) and IV (oxygen anion) apply.

5.4.3 Effective nonstoichiometry δ_{eff}

As already described above, the constraint from the substrate results in a reduced effective chemical expansion coefficient of $\varepsilon_{\text{eff}} = 0.18\%$. By using Eqs. (12)–(15), an oxygen nonstoichiometry of 0.020 is calculated from ε_{eff}. At elevated temperatures PCO thin films already exhibit an oxygen deficit δ_0 at ambient air that is $\delta_0 = 0.021$ for this calculation (see Appendix, Section A.3). Summed up, these oxygen non-stoichiometries result in an effective oxygen nonstoichiometry of $\delta_{\text{eff}} = 0.020 + 0.021 = 0.041$. This means that a PCO bulk sample at δ_{eff} exhibits a comparable volume expansion as our thin films at $\delta_{\text{II}} = 0.05$ which is the oxygen nonstoichiometry in the plateau region (II). For more details on δ_0 and δ_{II} see Appendix, Section A.3, or [32].

5.4.4 Cation and anion radii changes in the PCO thin films

The influence of the chemical expansion on the effective cation and anion radii change is already evident at the beginning of the LDV measurements, see column “δ_0” in Table 2. These are the radii in ambient air. For comparability, the radii for

Table 2: Influence of nonstoichiometry δ on effective cation and anion radii. The relative change of the radii with respect to δ_0 is given in brackets.

	$\delta = 0$	$\delta_0 = 0.021$	$\delta_{II} = 0.050$ (bulk PCO)	$\delta_{\mathrm{eff}} = 0.041$ (thin-film PCO)
r_{cation} [Å]	0.969	0.976	0.985 (+0.94%)	0.982 (+0.63%)
r_{anion} [Å]	1.380	1.378	1.375 (−0.22%)	1.376 (−0.15%)

$\delta = 0$ are given as well. As δ_0 represents the initial point of the LDV measurements, the following columns do not only show the calculated effective radii, but additionally the respective relative changes with respect to the radii at δ_0. The related radii changes for bulk and thin-film PCO are calculated by applying the values for δ_{II} (bulk) and δ_{eff} (thin film) to the model taken from [22]. The values calculated for δ_{II} (see Table 2) are the ones one would expect for an unrestrained bulk sample.

The thin-film radii changes are significantly smaller than those expected for an unrestrained bulk sample. However, at this point one should keep the geometry in mind. In the view of this model, the effective changes of the ion radii reflect changes in the space around a given cation or anion, i.e. anisotropic changes of the lattice constant. For an unconstrained bulk sample, the radii change is isotropic. Therefore, in a first approximation, one can assume that each direction (X, Y, Z) contributes to one third to the total volume expansion. In the thin-film case, the constraint from the substrate leads to anisotropic expansion. Nearly the whole volume expansion is directed along the Z axis. With this view in mind, the effective radii change perpendicular to the substrate plane is nearly double for the thin film as compared to the bulk sample. This is in good agreement with the prediction in [40] (see Eq. (4) in Section 2.2) where a thin film may show an enhanced chemical expansion of a factor of 1.67–2.0 along its unconstrained direction.

5.5 Reproducibility

Measurements, especially at low frequencies, are time consuming. One sample is often measured over several days and up to a few weeks to achieve a full data set that includes the dependencies on the excitation frequency, the excitation voltage and the temperature. This holds even more true if more than one data point per parameter set is measured; either to minimize the effect of external disturbances, for verification or also to scan several positions on the sample surface. Therefore, reproducibility and signal stability need to be addressed. They are critical when considering industrial applications. Reliability is a key issue as well, including thermal and mechanical (long-term) stability, as well as the

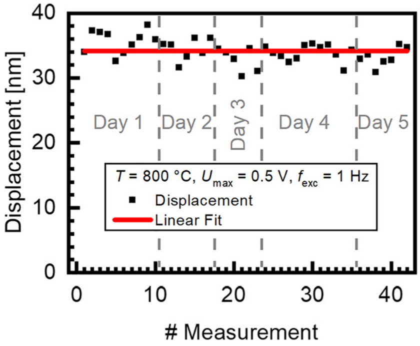

Figure 15: Reproducibility of sample displacement as obtained by high-temperature LDV. 42 measurements on five consecutive days were performed under the following identical conditions: $T = 800$ °C, $U_{max} = 0.5$ V, $f_{exc} = 1$ Hz.

reproducibility of the displacement. In this work, this aspect is considered over a 5-day-period (see Figure 14). A more detailed investigation on the long-term stability will be the subject of future research.

The results shown in Figure 15 allows one to evaluate the reproducibility of the thin-film PCO and the LDV setup. The temperature of 800 °C was chosen as it is the highest temperature addressed in this work. For investigating the reproducibility under more realistic conditions of operation, the thermal and mechanical stress to the sample was enhanced by heating up or cooling down the sample to different temperatures in between the measurements depicted in Figure 15. At these intermediate steps some of the measurements described in Sections 4.1–4.3 were performed under varying conditions (temperature, applied potential, excitation frequency).

Overall, very good stability with no significant degradation was found in 42 measurements, leading to a standard deviation of 7.8%. This agrees with prior research on the resolution of the LDV system [19]. For more information on the measurement uncertainty see Section A.4 in the Appendix.

6 Conclusions

The chemical expansion of PCO and undoped ceria thin films was investigated over a wide range of temperature (600–800 °C), excitation frequency (0.1–10 Hz) and excitation potential (0.25–0.75 V for PCO; 0.25–1.0 V for $CeO_{2-\delta}$), the latter equivalent to a change in oxygen partial pressure down to about 10^{-17} bar. At low frequencies, equilibrium conditions are approached, and the maximum thin-film expansion of the PCO film is expected given full reduction of the Pr ions. The total displacement of a constrained film includes two major contributions: the electrochemically induced film thickness change and the induced substrate/sample bending as illustrated in this study.

The LDV measurement, as a non-contact characterization method, has been demonstrated to be suitable for determining both film thickness change and total displacement, including bending. The latter enables displacement mapping and is used to indirectly determine thin-film thickness changes as well. Displacement dependencies on excitation frequency, temperature, excitation potential, and position on the sample were identified.

This work is the first systematic study of chemical expansion of doped and undoped ceria thin films including temperatures above 650 °C utilizing the high precision non-contact optical measurement method based on LDV. For PCO this means a significant extension of the data sets reported in the literature, especially, with respect to the higher temperatures. This also allowed for experimental data to be collected, for the first time, for both the direct film thickness changes as well as the induced substrate bending and their correlation for high temperatures of 750 °C and above. Here, it shall be pointed out that because the newly developed LDV system is not only capable of detecting displacements in oxide thin films with high chemical expansion coefficients, like PCO, but works as well for samples with low chemical expansion, it was possible to characterize chemical expansion for the first time, as well, for ceria thin films.

To approach equilibration of films, particularly at the lower measurement temperatures, excitation frequencies of 0.1 Hz or even lower were necessary. Currently, this appears to be a limiting factor in the application of the LDV method. Below 0.1 Hz, LDV measurements exhibited low signal-to-noise ratios, limiting the ability to obtain reliable chemical expansion data. Our LDV system is currently being upgraded to a two-beam diffraction system that is expected to allow access to much lower frequencies.

For PCO, a film thickness change of a few nanometers corresponds to a total substrate bending-related displacement of several hundred nanometers. For $\mathrm{PCO}_{\mathrm{edge}}$ a multiplication factor of $\xi \approx 45$ is found for the ratio of displacement to the length change of a free body. The LDV system exhibits a resolution for total displacement of 0.3 nm at 800 °C and 1 Hz, key for accessing chemical expansion in thin films that show little chemical expansion. In turn, this leads to a calculated detectable length change of a free body of only 5 pm. It is important to note that this value applies as well under the challenging conditions of elevated temperature exceeding 800 °C.

PCO thin films on YSZ substrates not only show remarkable displacements of several hundred nanometers even for voltages of less than 1 V. Combining this with the displacement reliability, PCO on YSZ appears to be a highly promising material combination for realizing a new generation of high-temperature actuators, by combining large reproducible displacements, high-temperature stability coupled with low energy consumption.

A defect model for bulk PCO was adapted to support the analysis of the experimental thin-film data. The film thickness change investigated in this work was correlated to oxygen nonstoichiometry data derived by nanogravimetry on comparable PCO thin films. This allowed us to calculate the effective volume expansions that correlate anisotropic volume changes in thin PCO films with isotropic volume changes in bulk PCO materials. The applied defect-chemical model correlates oxygen nonstoichiometry with volume change and effective cation and anion radii change. This allows for comparison of the different radii changes for thin film and bulk PCO under similar oxygen partial pressure conditions. Significant differences are identified between the isotropic change in PCO bulk specimens as reported in literature and PCO thin films as characterized in this work. The anisotropic volume expansion of the constrained thin film results in a film thickness change that is about double that obtained for bulk expansion.

Author contributions: All the authors have accepted responsibility for the entire content of this submitted manuscript and approved submission.

Research funding: HW, DK, CS, RM and HF gratefully acknowledge the financial support of the German Research Foundation (Deutsche Forschungsgemeinschaft; DFG) (grant nos. FR 1301/31-1, FR 1301/23-1 and MO 1060/29-1). In addition, the authors thank the Research Center Energy Storage Technologies (Forschungszentrum Energiespeichertechnologien) for supporting this work. HLT and TD thank the U.S. Department of Energy, Basic Energy Sciences Program: "Chemomechanics of Far-From-Equilibrium Interfaces" (COFFEI), project DE-SC0002633 for funding.

Conflict of interest statement: The authors declare no conflicts of interest regarding this article.

Appendix

A.1 Application of Stoney model

Chemical expansion induced bending of films driven by electrochemical titration is expected to reach a saturation value at low frequencies [18, 19, 30]. This trend is observed in Figures 12 and 13. For comparison, the maximum bending calculated by the Stoney model [58] using a bulk chemical expansion of 0.4% [15], is added to Figure 13 (dashed green line). For low frequencies and high temperatures, the thin-film data show nearly equal values as the bulk limit. This is not unexpected, since the thin-film chemical expansion coefficient for PCO exceeds its bulk expansion coefficient [40].

The Stoney equation describes a substrate/film system and correlates the radius of the substrate curvature R with the film stress $\Delta\sigma_f$. Since the substrate is much thicker than the film, the following approximation is valid [59]:

$$\Delta\sigma_\mathrm{f} = \frac{Y_\mathrm{s}\, t_\mathrm{s}^2}{6R(1-\nu_\mathrm{s})t_\mathrm{f}} \tag{16}$$

Here, Y is the Young's modulus, t the thicknesses of film or substrate, and ν the Poisson ratio. The subscripts s and f indicate substrate and film properties, respectively. The curvature radius R of the sample can be accessed by fitting a spherical surface segment to the experimental data.

Literature data for Y_s and ν_s of 330 GPa and 0.44, respectively, are taken from [60]. The data are reported for (100)-oriented 8 mol-% YSZ at 800 °C in ambient air. Using these data, the calculated curvature radius of 73 m for $\mathrm{PCO_{edge}}$ results in an in-plane stress of 270 MPa. This is in the same order of magnitude as the literature value of 460 MPa given in [42]. It should be mentioned that the data presented in [42] was obtained from PCO films deposited on single crystalline Al_2O_3 substrates and not on YSZ substrates as in this work. Considering that the Young's modulus for Al_2O_3 substrates is about 450 GPa [61] and thus significant higher than for PCO on YSZ, the deviation between this work and the given literature value for $\Delta\sigma_\mathrm{f}$ is further reduced.

This calculation for the in-plane film stress is an approximation only. Both, Y and ν, are temperature dependent material properties affected by the p_{O2}. Reliable data for the temperature dependence of Y and ν over a wide p_{O2} range are unfortunately incomplete. Additionally, $\Delta\sigma_\mathrm{f}$ will not remain at a constant value during the pumping cycle as the film continuously expands and contracts with its excitation frequency. Therefore, the actual stress is dependent on the oxygen activity and, thus, on the actual excitation potential which changes periodically. The calculations above are carried out for the maximum curvature radius and thus represent the sample's condition with the maximal displacement and the highest stress.

It can be easily seen, that the curvature radius R is inversely proportional to the bending b (compare Figure 14). Therefore, the following dependencies between the bending b and film t_f and substrate thickness t_s are derived from Eq. (16):

$$b \sim t_\mathrm{f} \tag{17}$$

and

$$b \sim 1/t_\mathrm{s}^2 \tag{18}$$

A.2 Correlation between chemical expansion of bulk and constrained thin films

The physical property that correlates thin-film expansion c_f with the length change of a free body consisting of the same material c_b is the Poisson number ν. Assuming the film is fully clamped to the substrate, the following relation applies between the chemical expansion coefficient ε_b of the bulk material and the chemical expansion coefficient ε_f of a thin film expanding only in one direction [40]:

$$\varepsilon_f = \varepsilon_b\left(\frac{1+\nu}{1-\nu}\right) - \frac{2\nu\sigma_0}{Y_s} \tag{19}$$

The second term describes a reference state from which an additional chemical expansion begins. It is calculated by the Young's modulus in the substrate Y_s and σ_o the stress in the film in the reference state.

It should be noted that the latter term is omitted in the current study as the LDV reflects dynamic changes of the expansion.

In this particular case this term is expected to result in $\sigma_o \approx 0$ anyway due to annealing of the samples.

As the chemical expansion describes dimensional changes c_i of the material in relation to its dimension t_i (film: i = f, bulk: i = b)

$$\varepsilon_f = \frac{c_f}{t_f} \quad ; \quad \varepsilon_b = \frac{c_b}{t_b} \tag{20}$$

Equation (19) simplifies with $t_f = t_b$ to:

$$c_f = c_b\left(\frac{1+\nu}{1-\nu}\right) \tag{21}$$

Typical Poisson numbers of (doped) ceria are around $\nu = 0.33$, resulting in an anisotropic film thickness change c_f that is about two times bigger than the length change of a free body c_b.

A.3 Oxygen-nonstoichiometry of PCO thin films characterized by piezoelectric nanobalance

At elevated temperatures, PCO already exhibits an oxygen deficiency in ambient air. Oxygen nonstoichiometry data for PCO thin films are taken from our previous investigations on similar specimens [32]. There, PCO thin films were characterized using a resonant nanobalance. A mass resolution of about 50 ng was achieved at 700 °C. For a film of 1 µm thickness, this equals to an uncertainty of $\Delta\delta = 0.005$.

A PCO film annealed to 700 °C in ambient air ($p_{O2} = 10^{-0.67}$ bar) showed an oxygen nonstoichiometry of $\delta_0 = 0.021$ which corresponds to the starting point of the present LDV measurements without an applied potential. At $p_{O2} = 10^{-8}$ bar, the oxygen nonstoichiometry rises to $\delta_{II} = 0.05$ which is in the plateau region (II). The difference, $\delta_{\mathrm{LDV}} = \delta_{\mathrm{II}} - \delta_{\mathrm{O}} = 0.029$ is the total change of oxygen nonstoichiometry evoked by the electrochemical pumping of the samples in this work.

A.4 Measurement uncertainty

To address measurement uncertainty, a set of comparative measurements was recorded for the $\mathrm{PCO_{edge}}$ sample. Figure 15 shows 42 measurements on five consecutive days performed under identical conditions (Temperature: 800 °C, excitation voltage: 0.5 V, excitation frequency: 1 Hz). The standard deviation between these measurements is calculated to be 7.6% and is taken as representative of the measurement uncertainty. While a number of factors have been identified as contributing to uncertainty, laboratory vibrations were found to have a strong negative impact on the signal-to-noise level and, thereby, to measurement data reproducibility.

In a prior research [19], the resolution of the LDV setup was investigated. It was found that displacements of $D = 20$ nm and $D = 10$ nm are measurable at 0.5 Hz and 1 Hz, respectively, if a tolerable relative difference $\Delta D/D \approx 20\%$ was chosen. This correlates well with the results of this work as the about three times higher displacement of 34 nm leads to deviations of only about a third of the estimated 20%. Therefore, it can be concluded that the main deviation of the data shown in Figure 15 originate from the measurement itself and not from possible fluctuations in the sample or the thin-film material.

References

1. Løken A., Ricote S., Wachowski S. Thermal and chemical expansion in proton ceramic electrolytes and compatible electrodes. *Crystals* 2018, *8*, 365–434.
2. Wu Y., Xu X., Yan Z., Zhong Z. Thermo-electro-chemo-mechanical modeling of solid oxide fuel cell for stress and failure evolution during duty cycle. *J. Electrochem. Soc.* 2021, *168*, 044511.
3. Bishop S. R., Marrocchelli D., Chatzichristodoulou C., Perry N. H., Mogensen M. B., Tuller H. L., Wachsman E. D. Chemical expansion: implications for electrochemical energy storage and conversion devices. *Annu. Rev. Mater. Res.* 2014, *44*, 205–239.
4. Zhang S., Xia R., Lebrun L., Anderson D., Shrout T. R. Piezoelectric materials for high power, high temperature applications. *Mater. Lett.* 2005, *59*, 3471–3475.
5. Lee H. J., Zhang S., Bar-Cohen Y., Sherrit S. High temperature, high power piezoelectric composite transducers. *Sensors* 2014, *14*, 14526–14552.
6. Moulson A. J., Herbert J. M. *Electroceramics: Materials, Properties, Applications–Chapter 6: Piezoelectric Ceramics*, 2nd ed.; John Wiley & Sons: Chichester, UK, 2003.
7. Shrout T. R., Zhang S. J. Lead-free piezoelectric ceramics: alternatives for PZT? *J. Electroceram.* 2007, *19*, 111–124.

8. Newnham R. E. *Properties of Materials: Anisotropy, Symmetry, Structure*; Oxford University Press: Oxford, UK, 2005.
9. Fachberger R., Bruckner G., Knoll G., Hauser R., Biniasch J., Reindl L. Applicability of $LiNbO_3$, langasite and $GaPO_4$ in high temperature SAW sensors operating at radio frequencies. *IEEE Trans. Ultrason. Ferroelectrics Freq. Control* 2004, *51*, 1427–1431.
10. Birnie D. P., III Analysis of diffusion in lithium niobate. *J. Mater. Sci.* 1993, *28*, 302–315.
11. Damjanovic D. Materials for high temperature piezoelectric transducers. *Curr. Opin. Solid State Mater. Sci.* 1998, *3*, 469–473.
12. Davulis P., Kosinski J., Cunha M. $GaPO_4$ stiffness and piezoelectric constants measurements using the combined thickness excitation and lateral field technique. *Proc. IEEE Int. Freq. Control Symp.* 2006, 664–669; https://doi.org/10.1109/FREQ.2006.275466.
13. Krempl P., Schleinzer G., Wallnöfer W. Gallium phosphate, $GaPO_4$: a new piezoelectric crystal material for high temperature sensorics. *EUROSENSORS* 1996, *10*, 1093–1096.
14. Worsch P., Krempl P., Krispel F., Reiter C., Thanner H., Wallnöfer W. The temperature-stable piezoelectric material $GaPO_4$ and its sensor applications. In Transducers ’01 Eurosensors XV 2001; pp. 1006. https://doi.org/10.1007/978-3-642-59497-7_231.
15. Bishop S. R., Tuller H. L., Kuru Y., Yildiz B. Chemical expansion of nonstoichiometric $Pr_{0.1}Ce_{0.9}O_{2-\delta}$: correlation with defect equilibrium model. *J. Eur. Ceram. Soc.* 2011, *31*, 2351–2356.
16. Hong S. J., Virkar A. V. Lattice parameters and densities of rare-earth oxide doped ceria electrolytes. *J. Am. Ceram. Soc.* 1995, *78*, 433–439.
17. Chatzichristodoulou C., Hendriksen P. V., Hagen A. Defect chemistry and thermomechanical properties of $Ce_{0.8}Pr_xTb_{0.2-x}O_{2-\delta}$. *J. Electrochem. Soc.* 2010, *157*, B299–B307.
18. Swallow J. G., Kim J. J., Maloney J. M., Chen D., Smith J. F., Bishop S. R., Tuller H. L., Van Vliet K. J. Dynamic chemical expansion of thin-film non-stoichiometric oxides at extreme temperatures. *Nat. Mater.* 2017, *16*, 749–755.
19. Schmidtchen S., Fritze H., Bishop S. R., Chen D., Tuller H. L. Chemical expansion of praseodymium-cerium oxide films at high temperatures by laser Doppler vibrometry. *Solid State Ionics* 2018, *319*, 61–67.
20. Bishop S. R., Duncan K. L., Wachsman E. D. Thermo-chemical expansion of SOFC materials. *ECS Trans.* 2006, *1*, 13–21.
21. Wang S., Oikawa E., Hashimoto T. Structural analysis of $Ce_{1-x}M_xO_{2-0.5x-\delta}$ (M = Gd, Sm, Y) by high temperature XRD under various oxygen partial pressures. *J. Electrochem. Soc.* 2004, *151*, E46–E50.
22. Marrocchelli D., Bishop S., Tuller H. L., Yildiz B. Understanding chemical expansion in non-stoichiometric oxides: ceria and zirconia case studies. *Adv. Funct. Mater.* 2012, *22*, 1958–1965.
23. Schmidtchen S. *Aufbau eines Laser-Vibrometer-Messsystems zur Hochtemperatur-Charakterisierung von Sensorkomponenten.* Ph.D. Thesis, Clausthal University of Technology, Clausthal, Germany, 2013.
24. Chiang H. W., Blumenthal R. N., Fournelle R. A. A high-temperature lattice-parameter and dilatometer study of the defect structure of nonstoichiometric cerium dioxide. *Solid State Ionics* 1993, *66*, 85–95.
25. Mogensen G., Mogensen M. Reduction reactions in doped ceria ceramics studied by dilatometry. *Thermochim. Acta* 1993, *214*, 47–50.
26. Hull S., Norberg S. T., Ahmed I., Eriksson S. G., Marrocchelli D., Madden P. A. Oxygen vacancy ordering within anion-deficient ceria. *J. Solid State Chem.* 2009, *182*, 2815–2821.

27. Brauer G., Gingerich K. A. Über die Oxyde des Cers–V: Hochtemperatur-Röntgenuntersuchungen an Ceroxyden. *J. Inorg. Nucl. Chem.* 1960, *16*, 87–99.
28. Schmitt R., Nenning A., Kraynis O., Korobko R., Frenkel A. I., Lubomirsky I., Haile S. M., Rupp J. L. M. A review of defect structure and chemistry in ceria and its solid solutions. *Chem. Soc. Rev.* 2020, *49*, 554–592.
29. Kuru Y., Bishop S. R., Kim J. J., Yildiz B., Tuller H. L. Chemomechanical properties and microstructural stability of nanocrystalline Pr-doped ceria: an in situ X-ray diffraction investigation. *Solid State Ionics* 2011, *193*, 1–4.
30. Panlener R. J., Blumenthal R. N., Garnier J. E. A thermodynamic study of nonstoichiometric cerium dioxide. *J. Phys. Chem. Solid.* 1975, *36*, 1213–1222.
31. Kogut I., Wollbrink A., Steiner C., Wulfmeier H., El Azzouzi F.-E., Moos R., Fritze H. Linking the electrical conductivity and non-stoichiometry of thin film $Ce_{1-x}Zr_xO_{2-\delta}$ by a resonant nanobalance approach. *Materials* 2021, *14*, 748.
32. Schröder S., Fritze H., Bishop S., Chen D., Tuller H. L. Thin-film nano-thermogravimetry applied to praseodymium-cerium oxide films at high temperatures. *Appl. Phys. Lett.* 2018, *112*, 213502.
33. Bishop S. R., Stefanik T. S., Tuller H. L. Defects and transport in $Pr_xCe_{1-x}O_{2-\delta}$: composition trends. *J. Mater. Res.* 2012, *27*, 2009–2016.
34. Chen D., Tuller H. L. Voltage-controlled nonstoichiometry in oxide thin films: $Pr_{0.1}Ce_{0.9}O_{2-\delta}$ case study. *Adv. Funct. Mater.* 2014, *24*, 7638–7644.
35. Kuhn M., Bishop S. R., Rupp J. L. M., Tuller H. L. Structural characterization and oxygen nonstoichiometry of ceria-zirconia ($Ce_{1-x}Zr_xO_{2-d}$) solid solutions. *Acta Mater.* 2013, *61*, 4277–4288.
36. Bishop S. R., Duncan K. L., Wachsman E. D. Defect equilibria and chemical expansion in non-stoichiometric undoped and gadolinium-doped cerium oxide. *Electrochim. Acta* 2009, *54*, 1436–1443.
37. McBride J. R., Hass K. C., Poindexter B. D., Weber W. H. Raman and X-ray studies of $Ce_{1-x}RE_xO_{2-y}$, where RE=La, Pr, Nd, Eu, Gd, and Tb. *J. Appl. Phys.* 1994, *76*, 2435–2441.
38. Duncan K., Wang Y., Bishop S. R., Ebrahimi F., Wachsman E. D. The role of point defects in the physical properties of nonstoichiometric ceria. *J. Appl. Phys.* 2007, *101*, 044906.
39. Minervini L., Zacate M. O., Grimes R. W. Defect cluster formation in M_2O_3-doped CeO_2. *Solid State Ionics* 1999, *116*, 339–349.
40. Bishop S. R., Chen D., Sheth J., Misture S. T., Sheldon B. W., Kim J. J., Tuller H. L. Impact of size scale on electro-chemo-mechanical coupling properties in MIECs: bulk and thin film (Pr,Ce) $O_{2-\delta}$. *ECS Trans.* 2014, *61*, 31–36.
41. Chen D., Bishop S. R., Tuller H. L. Non-stoichiometry in oxide thin films: a chemical capacitance study of the praseodymium-cerium oxide system. *Adv. Funct. Mater.* 2013, *23*, 2168–2174.
42. Sheth J., Chen D., Kim J. J., Bowman W. J., Crozier P. A., Tuller H. L., Misture S. T., Zdzieszynski S., Sheldon B. W., Bishop S. R. Coupling of strain, stress, and oxygen non-stoichiometry in thin film $Pr_{0.1}Ce_{0.9}O_{2-\delta}$. *Nanoscale* 2016, *8*, 16499–16510.
43. Chatzichristodoulou C., Hendriksen P. V. Oxygen nonstoichiometry and defect chemistry modeling of $Ce_{0.8}Pr_{0.2}O_{2-\delta}$. *J. Electrochem. Soc.* 2010, *157*, B481–B489.
44. Kawada T., Suzuki J., Sase M., Kaimai A., Yashiro K., Nigara Y., Mizusaki J., Kawamura K., Yugamic H. Determination of oxygen vacancy concentration in a thin film of $La_{0.6}Sr_{0.4}CoO_{3-\delta}$ by an electrochemical method. *J. Electrochem. Soc.* 2002, *149*, E252–E259.

45. Chen D., Bishop S. R., Tuller H. L. Nonstoichiometry in oxide thin films operating under anodic conditions: a chemical capacitance study of the praseodymium–cerium oxide system. *Chem. Mater.* 2014, *26*, 6622–6627.
46. Chen D., Bishop S. R., Tuller H. L. Nonstoichiometry in oxide thin films operating under anodic conditions: a chemical capacitance study of the praseodymium–cerium oxide system. *Adv. Funct. Mater.* 2013, *23*, 2168–2174.
47. Spiridigliozzi L., Dell'Agli G., Marocco A., Accardo G., Pansini M., Yoon S. P., Ham H. C., Frattini D. Engineered co-precipitation chemistry with ammonium carbonate for scalable synthesis and sintering of improved $Sm_{0.2}Ce_{0.8}O_{1.90}$ and $Gd_{0.16}Pr_{0.04}Ce_{0.8}O_{1.90}$ electrolytes for IT-SOFCs. *J. Ind. Eng. Chem.* 2018, *59*, 17–27.
48. Kogut I., Steiner C., Wulfmeier H., Wollbrink A., Hagen G., Moos R., Fritze H. Comparison of the electrical conductivity of bulk and film $Ce_{1-x}Zr_xO_{2-\delta}$ in oxygen-depleted atmospheres at high temperatures. *J. Mater. Sci.* 2021, *56*, 17191–17204.
49. Richter D., Sakharov S., Forsén E., Mayer E., Reindl L., Fritze H. Thin film electrodes for high temperature surface acoustic wave devices. *Procedia Eng.* 2011, *25*, 168–171.
50. Kim S., Fleig J., Maier J. Space charge conduction: simple analytical solutions for ionic and mixed conductors and application to nanocrystalline ceria. *Phys. Chem. Chem. Phys.* 2003, *5*, 2268–2273.
51. Chen D., Bishop S. R., Tuller H. L. Praseodymium-cerium oxide thin film cathodes: study of oxygen reduction reaction kinetics. *J. Electroceram.* 2012, *28*, 62–69.
52. Nenning A., Opitz A. Low oxygen partial pressure increases grain boundary ion conductivity in Gd-doped ceria thin films. *J. Phys. Energy* 2020, *2*, 014002.
53. Kilo M., Argirusis C., Borchardt G., Jackson R. A. Oxygen diffusion in yttria stabilised zirconia – experimental results and molecular dynamics calculations. *Phys. Chem. Chem. Phys.* 2003, *5*, 2219–2224.
54. Kumari N., Anjum U., Haider M. A., Basu S. Oxygen anion diffusion in doped ceria $M_xCe_{1-x}O_{2-0.5x}$ (M=Gd, Sm and Pr): a molecular dynamics simulation study. *MRS Adv.* 2019, *4*, 783–792.
55. Wang S., Katsuki M., Hashimoto T., Dokiya M. Expansion behavior of $Ce_{1-y}Gd_yO_{2.0-0.5y-d}$ under various oxygen partial pressures evaluated by HTXRD. *J. Electrochem. Soc.* 2003, *150*, A952–A958.
56. Kalinin S., Balke N., Jesse S., Tselev A., Kumar A., Arruda T. M., Guo S., Proksch R. Li-ion dynamics and reactivity on the nanoscale. *Mater. Today* 2011, *14*, 548–558.
57. Shannon R. D. Revised effective ionic radii and systematic studies of interatomic distances in halides and chalcogenides. *Acta Crystallogr.* 1976, *A32*, 751–767.
58. Stoney G. G. The tension of metallic films deposited by electrolysis. *Proc. Roy. Soc. Lond. A* 1909, *82*, 172–175.
59. Ohring M. *Materials Science of Thin Films*, 2nd ed.; Academic Press: Hoboken, NJ, 2001; pp 727–730.
60. Zhou J., Zhang J., Zhong Z. Mechanical properties of yttria-stabilized zirconia: a study by ReaxFF molecular dynamics simulations. *Mech. Mater.* 2020, *149*, 103542.
61. Salem J. A., Li Z., Bradt R. C. *Thermal Expansion and Elastic Anisotropy in Single Crystal* Al_2O_3 *and SiC Reinforcements*; NASA Technical Memorandum, 1986; pp 106516.